MÖSSBAUER SPECTROSCOPY AND X–RAY DIFFRACTION STUDY OF (Cd, Zn) SUBSTITUTED MIXED FERRITES

by

JUSTICE ZAKHELE MSOMI

BSc, BSc(Hons) (UDW)

Submitted in fulfilment of the academic requirements for the degree of Master of Science in the School of Pure & Applied Physics, University of Natal, Durban.

August 2002

Acknowledgments

I thank the following people for their contributions and sacrifices as indicated below to make this work a success:

- Dr T. Moyo for invaluable supervision, guidance and encouragement throughout the period of this work.

- Prof T. B. Doyle for many ideas and invaluable sacrifices and inputs throughout the period of this work.

- Prof K. Bharuth–Ram for valuable discussions and assistance in the analysis of Mössbauer results using Recoil Mössbauer software package.

- Staff members in the Physics Workshop for their prompt attention to all aspects of designing and maintenance of the experimental apparatus used in this work and my fellow research students in the School of Pure and Applied Physics for their encouragement and support at all times.

My final thanks are reserved for members of my family for their encouragement, and for my friend, Lungile Ngidi, for her support and understanding.

Dedication

In memory of my father, Isiah Msomi

Declaration

The candidate wishes to confirm that work described in this dissertation was carried out by the author in the School of Pure and Applied Physics at University of Natal. This is original work by the author and has not been submitted in any form to another University or institution. Credit has been given where use of the work of others is made.

J. Z. Msomi

August 2002

Abstract

The study of magnetic properties and structures of Zn and Cd substituted mixed ferrites has been carried out using Mössbauer spectroscopy and X–ray diffraction on powdered samples at about 300 K. Two series of mixed ferrites, $(Cd, Zn)_xCo_{1-x}Fe_{2-x}Al_xO_4$ and $(Cd, Zn)_xCo_{0.9}Fe_{1.7-x}Ti_{0.4}O_4$ (where $0 \leq x \leq 1.0$) were synthesized. In the former series the effect of simultaneous site dilution by Zn or Cd and Al atoms on tetrahedral (A) and octahedral (B) sites is investigated and in the latter the effect of single site dilution by Zn or Cd is also studied. The Mössbauer spectra show that the compounds transform with increase in x from ordered to disordered magnetic states. Systematic decrease in the hyperfine fields indicating weakening of the magnetic coupling with an increase in x is observed. We report the presence of a cross over effect with respect to the hyperfine fields on A and B sites at low concentration of diamagnetic ions in the simultaneously diluted series. Both series of compounds show no significant changes in isomer shifts with x. Differences in the evolution of Fe atoms on A and B sites between Zn and Cd based compounds are observed. The results of our analysis show that Zn and Cd ions occupy both tetrahedral and octahedral sites. The spinel structure of the compounds studied in this work is confirmed by X–ray diffraction (XRD). The lattice parameters derived from XRD show systematic change with x consistent with Vergard's law. In Cd based samples an increase of the lattice parameter with x is explained on the basis of the size difference of the cations involved. However, an anomalous behavior of the lattice parameter is observed in Zn based samples. The average grain sizes of the samples were determined from the line width of the (311) XRD intensity lines using the Scherrer formula. These vary between 50 nm and 70 nm for all the samples except for Zn and Al substituted samples which show a systematic anomalous reduction for $x \geq 0.4$ in grain size. The porosity, x–ray and bulk densities of the samples are also presented.

Publications based on the current work

1. Mössbauer and XRD study of (Cd, Zn)$_x$Co$_{1-x}$Fe$_{2-x}$Al$_x$O$_4$ spinel ferrites
   J. Z. Msomi, T. Moyo and K. Bharuth-Ram, Hyperfine Interactions (2002) (accepted for publication).

2. Magnetic relaxation in (Cd, Zn)$_x$Co$_{0.9}$Fe$_{1.7-x}$Ti$_{0.4}$O$_4$ spinel oxides
   T. Moyo, J. Z. Msomi, and K. Bharuth-Ram, Hyperfine Interactions 136 (3) (2001) 579.

Contents

List of Figures

List of Tables

Chapter 1

Introduction to ferrites

Ferrites are oxides which possess the structure of the mineral spinel, $MgAl_2O_4$ [1]. Their chemical formula take the form AB_2O_4, where A and B are metal cations on the tetrahedral (A) and octahedral (B) sites. In simple ferrites, aluminium and magnesium ions in a spinel are replaced by iron and divalent metallic ions respectively. The chemical formula therefore takes the form MFe_2O_4 where M represents a divalent metal ion with an ionic radius in the range 0.06 nm to 0.1 nm [1]. A mixed ferrite consists of a combination of metal ions with $ZnFe_2O_4$ and $Zn_{0.5}Co_{0.5}Fe_2O_4$ examples of simple and mixed ferrites respectively.

In this chapter some details of the crystal structure, magnetic ordering and magnetic interactions in ferrites are discussed. A brief account of the motivation for the present study is also presented.

1.1 Crystal structure

The spinel structure is illustrated in figure 1.1. The unit cell is made up of eight of these cubes and which crystallize in a cubic system. The structure may be regarded as a face–centered cubic lattice of oxygen ions. In this closely packed oxygen lattice there are two kinds of interstitial sites called (A) and (B) sites, where metal cations occupy these interstitial sites. The position of the B site is

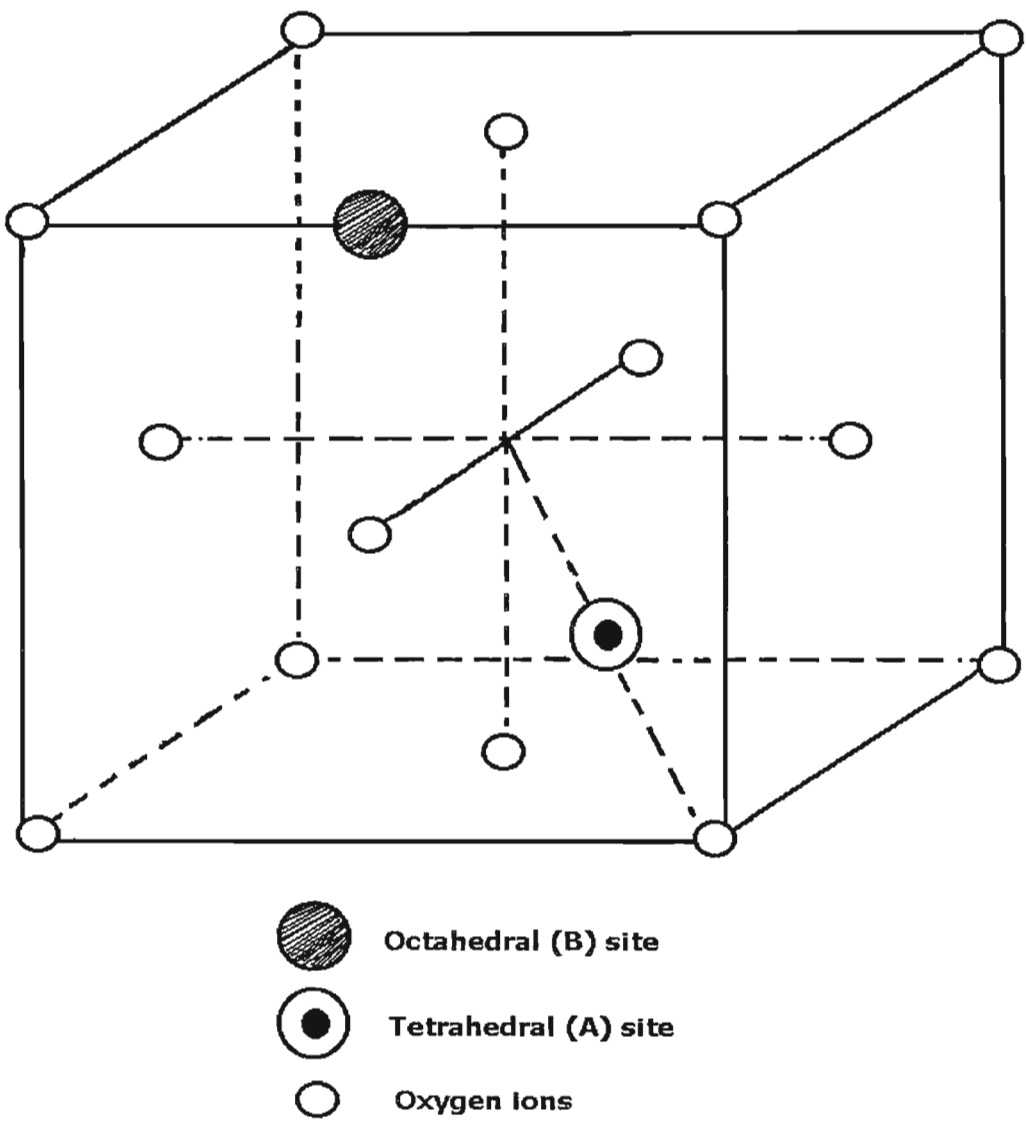

Figure 1.1: Schematic diagram of one eighth of the unit cell of the spinel structure [4].

at the center of a cube edge and the A site is on the cube diagonal. The A site ions have four oxygen ions for neighbors forming a tetrahedron and the B site ions are surrounded by six neighbors forming an octahedron [1]. We therefore speak of tetrahedral (A) and octahedral (B) sites. The cubic symmetry results in a low electric field gradient on a A site compared to the trigonal symmetry on a B site. This results in higher quadrupole splitting on an octahedral (B) site compared to a tetrahedral (A) site in ferrites [2, 3].

The general distribution of metal cations on A and B sites is given by [1]

$$\left(M_{\sigma}^{2+}\mathrm{Fe}_{1-\sigma}^{3+}\right)^{\mathrm{A}}\left(M_{1-\sigma}^{2+}\mathrm{Fe}_{1+\sigma}^{3+}\right)^{\mathrm{B}}\mathrm{O}_4 \tag{1.1.1}$$

where σ represents the degree of inversion. For completely normal and inverse spinels $\sigma = 1$ and $\sigma = 0$ respectively giving extreme cases. In a completely normal spinel all divalent ions occupy A sites and the trivalent ions B sites (see Figure 1.2 (a)). Cadmium ($CdFe_2O_4$) and zinc ($ZnFe_2O_4$) ferrites are normal spinels [2, 5] with all Cd^{2+} and Zn^{2+} ions on A sites and all Fe^{3+} ions on B sites. In a completely inverse spinel, A sites are not occupied by divalent ions but by trivalent ions. Half of B sites are occupied by divalent ions and the other half by the remaining trivalent ions (see Figure 1.2 (b)). Cobalt ferrite ($CoFe_2O_4$) and magnetite (Fe_3O_4) are inverse spinels [1, 5]. In these spinels all Co^{2+} and Fe^{2+} ions occupy B sites and A sites are occupied by Fe^{3+} ions.

Ferrimagnetic spinels are more or less inverse. The measure of inversion (σ) tends to depend on the method of preparation of samples [4]. Cations also tend to have site preferences and depends on factors like ionic size and electronic configuration of the cations. Cations with smaller size prefer to occupy tetrahedral sites while larger cations have more preference for octahedral sites. This is because tetrahedral sites are smaller than octahedral sites [1]. Zn^{2+} and Cd^{2+} ions have been observed to show more preference for A sites where their 4s,p and 5s,p electrons respectively form covalent bonds with six 2p electrons of oxygen ions [1].

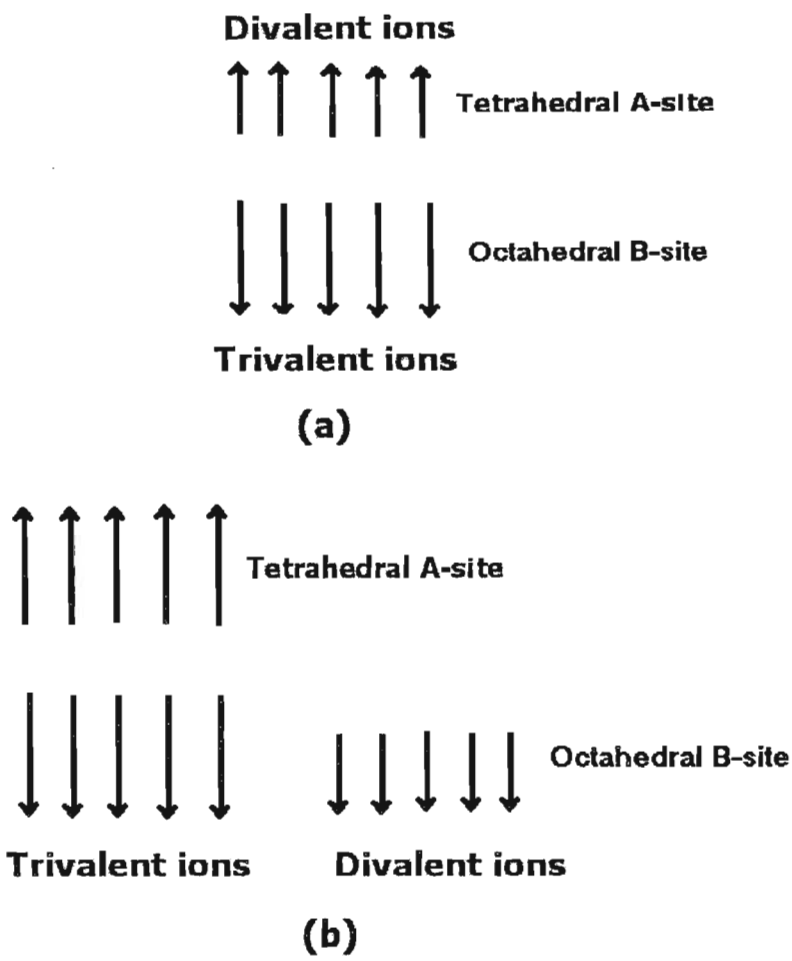

Figure 1.2: Spin arrangements on: (a) a normal spinel; (b) Fe ions in magnetite having an inverse spinel structure [4].

1.2 Magnetic ordering in magnetic materials

In ferromagnetic materials the interactions between neighboring magnetic moments are positive. This favors parallel alignment of the magnetic moments (see Figure 1.3 (a)). In the case of antiferromagnetic materials the interactions between the neighboring magnetic moments are negative. This tends to align the moments anti–parallel, resulting in a zero net magnetization as illustrated in Figure 1.3 (b). A special case of antiferromagnetism is ferrimagnetism, which occurs in ferrites. For a ferrimagnet, magnetic moments are ordered antiferromagnetically but in this case there are two unequal and anti-parallel systems of magnetic moments (see Figure 1.3 (c)). Thus a resultant magnetization occurs due to difference in magnitude of magnetic moments.

The ordering of magnetic moments depends on temperature, magnetic neighbors in the lattice and their separation. As the temperature or dilution of magnetic neighbors increases the magnetic phase usually changes from an ordered to a disordered phase. The magnetic phase in $Mn_xZn_{1-x}Fe_2O_4$ changes from disordered to an ordered phase with an increase in x because magnetic cations such as Mn^{2+} are replaced by nonmagnetic Zn^{2+} cations, resulting in a diluted magnetic environment [2]. The magnetic phase in $Zn_xCo_{1-x}Fe_2O_4$ changes from ordered to a disordered magnetic phase with increase in x as nonmagnetic Zn^{2+} replace magnetic Co^{2+} ions [6]. As the temperature is increased, transition from an ordered to a disordered magnetic phase takes place. This transition occurs at a certain critical temperature called the Curie point in ferro– and ferri– magnets.

A magnetic phase where the magnetic moments are randomly orientated (disordered), is called a paramagnetic state. This phase appears above the Curie temperature and occurs in materials having a high concentration of diamagnetic ions. Paramagnetism also occurs in a system of non–interacting or weakly interacting magnetic moments.

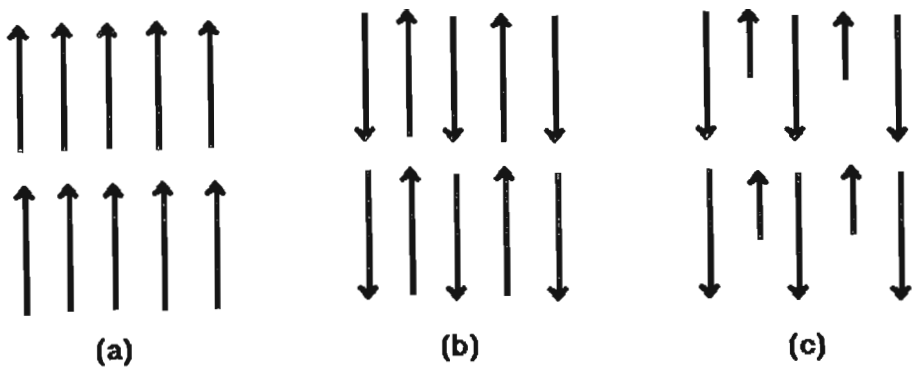

Figure 1.3: Schematic representation of spin: (a) ferromagnetism; (b) antiferromagnetism; (c) ferrimagnetism [4].

1.3 Magnetic interactions in ferrites

The major magnetic interactions in ferrites are between the A and B site cations (inter-sublattice interactions). The A–A and the B–B (intra–sublattice) interactions are much weaker because the interaction between any two magnetic ions X and Y in ferrites depends more upon the X–O–Y bond angle than the X-Y distance. It is a maximum for those ions X and Y for which the bond angle X–O–Y is closest to 180^o. Since the A site ions are antiparallel to B site ions in the spinel structure, the inter–sublattice interactions far exceed the intra–sublattice interactions. As a result, many of the spinels can order ferrimagnetically [2]. The A–B exchange interaction may involve both Fe–Fe or Fe–M interactions, where M is another paramagnetic cation. The distance between the metal cations on A and B sites is too big for a direct interaction to occur thus it takes place via an intermediate oxygen ion and is called super–exchange interaction [1]. The strength of the magnetic interaction in ferrites depends on the magnetic neighbors present in the Fe environment and is proportional to the Curie temperature [2].

The inter-sublattice and intra-sublattice interactions are represented by exchange integrals J_{AB} and J_{AA} and J_{BB}, respectively. When both J_{AA} and J_{BB} $\ll J_{AB}$, ferrimagnetic ordering appears in which A and B magnetic sublattices

are anti-parallel and occurs at low concentrations of diamagnetic ions in substituted mixed ferrites. This is because at low concentrations of diamagnetic ions, there are more exchange paths available and thus magnetic moments on A and B sites interact strongly. When magnetic cations are substituted by diamagnetic cations, the exchange paths are broken, resulting in weaker inter-sublattice interactions. This is considered to be the cause of weakening of the hyperfine fields in Mössbauer spectra [5, 6, 8, 9]. When it becomes comparable to the intra-sublattice interaction, A and B sublattices no longer remain anti-parallel, but become non-collinear. This phenomenon is explained by Bercoff et al [10] where the intra–sublattice interactions on each site tends to align spins antiferromagnetically while the inter–sublattice interaction tends to couple spins on A and those on B sites antiferromagnetically. This results in a disordered spin state and is revealed by paramagnetic doublets in the Mössbauer spectra. Therefore the nature and strength of the exchange interaction can be changed by diluting magnetic ions.

1.4 Motivation for current work

Ferrites are important magnetic materials in many practical applications [11–15] and are widely used in industry for their soft and hard magnetic properties. Those with soft magnetic properties are used in electrical–power applications. Manganese ferrites are widely used in electronic applications such as transformers, choke coils, noise filters and recording media. Nickel substituted zinc ferrites are commercially used as high frequency ferrites for radio frequency coils and transformer cores. Lithium ferrites are used in microwave applications. Ferrites with hard magnetic properties are used to make permanent magnets. Barium ferrites are largely used to make permanent magnets because of their low cost and good magnetic properties. The range and properties of ferrite materials is very wide. Some ferrites are also used in surface mounting technology in the electronic industry. This is important in the miniaturization

and densification of electronic components. Any systematic study of ferrite materials is therefore important.

The main objective of this work is to carry out a systematic study of magnetic properties of Cd or Zn substituted mixed ferrites in order to:

- investigate the site occupation of Cd or Zn and validity of simultaneous site dilution of A and B sites in the spinel structure.
- investigate the effect of size difference between Cd and Zn ions on magnetic properties.

The interest in this study stems from the fact that the distribution of cations in ferrites is random. Randomness and frustration have remarkable effects on magnetic properties and making suitable substitutions with diamagnetic ions can improve magnetic properties. As a result, several reports associated with substitutions by diamagnetic ions on tetrahedral (A) and octahedral (B) sites have appeared in the literature recently [3, 5, 6, 8, 9, 16–24].

Zn^{2+} and Cd^{2+} have been used extensively in substituted mixed ferrites and have generally been assumed to occupy A site only. In the study of magnetic properties of mixed ferrites in the series $Cd_xCo_{1-x}Fe_2O_4$ [5] and $Zn_xCo_{1-x}Fe_2O_4$ [6] ($0 \leq x \leq 1.0$), Fe^{3+} was found to migrate to a B site while Cd or Zn occupied A sites with an increase in x. Cobalt ferrite changed from ferrimagnetic to paramagnetic phase with increase in x. In the above cases dilution with diamagnetic ions is on a single site (A site). Thanki et al [8] have attempted to investigate the effect of diluting simultaneously the A and B sites by Zn and Al, on magnetic properties of a cobalt ferrite. The change from an ordered to a disordered magnetic state and relaxation effects have been found to take place faster (at about $x = 0.5$) compared to single site dilution. Thanki et al [8] assumed a general cation distribution of the form

$$\left(Zn_x^{2+}Fe_{1-x}^{3+}\right)^{A}\left(Co_{1-x}^{2+}Fe_{1.0}^{3+}Al_x^{3+}\right)^{B}O_4^{2-} \tag{1.4.1}$$

which confines Zn^{2+} ions to A site only. A compound of the series $Zn_xCo_{0.9}Fe_{1.7-x}Ti_{0.4}O_4$ at $x = 0.5$ ($Zn_{0.5}Co_{0.9}Fe_{1.2}Ti_{0.4}O_4$) was studied by Singh

et al [16] where a spin glass behavior was reported. Zn^{2+} ions were assumed to occupy the A sites only. In a study of compounds of the same series of the variation of magnetic properties as a function of composition (x = 0, 0.2 and 0.5) by Moyo et al [17], there was an indication that Zn^{2+} ions could be distributed on both the A and B sites. It is in this light that a systematic study of the composition dependence of magnetic properties of substituted mixed ferrites has been carried out in order to investigate the site occupation of Zn and Cd ions. Zn and Cd atoms have similar electronic configurations, but different ionic sizes. It is interesting to see the effect of size differences on magnetic properties and structure of the compounds.

A systematic Mössbauer spectroscopy and X–ray powder diffraction study on a complete series of compounds (Cd, Zn)$_x$Co$_{1-x}$Fe$_{2-x}$Al$_x$O$_4$ and (Cd, Zn)$_x$Co$_{0.9}$Fe$_{1.7-x}$Ti$_{0.4}$O$_4$ (where 0 $\leq x \leq$1.0, x in steps of 0.1 or 0.05) was conducted. ^{57}Fe Mössbauer spectroscopy was used to study the magnetic properties of the compounds because this technique provides detailed information of the changes in magnetic phases and site occupation of metal cations. The main difference between the samples investigated and those studied by Thanki et al [8] is that the present samples were prepared in flowing oxygen instead of air. The effect of flowing oxygen during sample preparation is also investigated in this work.

Mössbauer spectroscopy has been used extensively in the present study. Therefore it is appropriate to present some fundamentals of this technique.

Chapter 2

Principles of Mössbauer Spectroscopy

The study of recoilless nuclear resonant absorption or fluorescence is more commonly known as Mössbauer effect. It is a very accurate and sensitive way of obtaining information about chemical systems and can provide information on magnetic, structural, bonding, time dependent and other dynamical properties of materials. It is also able to detect variations in interaction energies between the appropriate probe nucleus and its surrounding electrons and thus provides information on hyperfine interactions. The basic principles of this spectroscopic technique are discussed in this chapter.

2.1 The Mössbauer effect

The Mössbauer effect is the resonant absorption or emission of γ–rays in a solid matrix without any energy degradation by recoil or thermal broadening and was discovered by Rudolf Mössbauer in 1957. Its direct application in the study of chemical systems arises from the availability of monochromatic electromagnetic radiation with a very narrowly defined energy spectrum that can be used to detect slight variations in the interaction energy between the nucleus and extra–nuclear electrons.

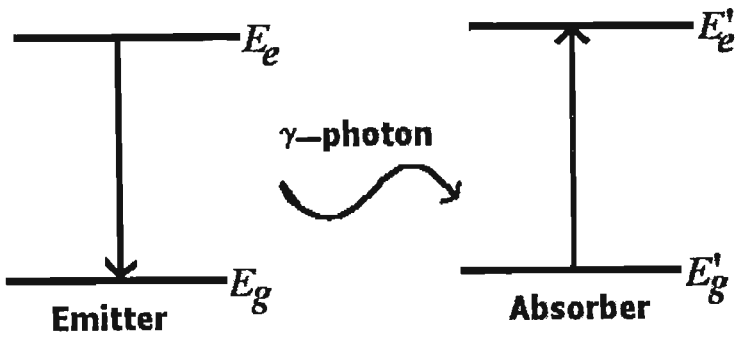

Figure 2.1: Emission and absorption of a γ–ray photon.

The Mössbauer effect involves transition of a γ–ray of energy E_γ. This can be considered through a system of two nuclei (see Figure 2.1) where one nucleus emits a γ–ray photon with energy $E_\gamma = E_e - E_g$ during the transition from an excited state with energy E_e to a ground state with energy E_g. Another nucleus absorbing this photon would make a transition from the ground state with energy E'_g to an excited state with energy E'_e. The condition for resonance between emitter and absorber nucleus would be met if $E_e - E_g = E'_e - E'_g$. This is expected to be the case for identical nuclei. Unfortunately, the effects of nuclear recoil and thermal energy degrade the energy of an emitted photon and does not match the transition energy of the absorber. This becomes clearer if a free nucleus of mass m moving with velocity V_x is considered as a photon of energy E_γ is emitted. Conservation of energy and momentum in the emission process gives the recoil energy of the nucleus

$$E_R = \frac{E_\gamma^2}{2mc^2}. \tag{2.1.1}$$

Its thermal or Doppler energy is given by

$$E_D = \pm mvV_x \tag{2.1.2}$$

where v is the change in speed of the nucleus after emission. Since the speeds v and V_x are smaller than the speed of light, non–relativistic mechanics can be applied. It can easily be shown [25] that the average Doppler energy is given

by

$$\overline{E_D} = E_\gamma \sqrt{\frac{k_B T}{mc^2}} \tag{2.1.3}$$

where k_B is the Boltzmann's constant, T is the absolute temperature and c the velocity of light. Equations (2.1.1) and (2.1.3) indicate that both recoil and Doppler energies are proportional to the energy E_γ. Therefore these quantities can be minimized for low energy γ–rays. Furthermore, the temperature dependence of the Doppler energy revealed by equation (2.1.3) indicates that the Doppler energy is minimum at low temperature. For a 14.41 keV transition in ^{57}Fe, the recoil energy is 1.95×10^{-6} keV and the Doppler energy is 1.0×10^{-5} keV at room temperature [25]. Therefore, when a nucleus is free, it loses energy E_R due to recoil when emitting a photon. For this photon to be reabsorbed by another nucleus, a further increment of energy by E_R above the transition energy is required. The recoil energy can be compensated partially by providing the nucleus with a high Doppler velocity ($\sim 7 \times 10^5$ mm/s) [25]. This method results in a marginal increase in the resonant overlap between emission and absorption spectra.

The Mössbauer effect eliminates the effects of recoil and thermal broadening because the recoiling nucleus is no longer free, but fixed on a solid lattice. In this case an emitting nucleus is held by strong bonding forces and the entire solid takes up the recoil energy. The mass m in equations (2.1.1) and (2.1.3) represents the total mass of the sample. Since this mass usually corresponds to at least 10^{15} atoms [25], the recoil energy, E_R, and the Doppler energy, E_D, become very small. However, nuclei are not completely rigidly bound and are free to vibrate. If the recoil energy is not taken up by the whole sample, it will be transferred to the lattice by increasing its vibrational energy. In this case the nuclei dissipate recoil energy by creation of phonons. The recoil energy is only transferred to lattice vibrations if it corresponds closely with allowed increments, otherwise it is transferred to a crystal as a whole ensuring negligible recoil energy and zero phonons created. The recoilless fraction f is related to

the vibrational properties of the crystal lattice by [2]

$$f = exp\left(-\frac{E_\gamma^2 < x^2 >}{(\hbar c)^2}\right) \tag{2.1.4}$$

where $< x^2 >$ is the component of the mean-square vibrational amplitude of the emitting atom in the direction of the γ–ray. To increase the recoilless resonance, f must be as large as possible. The form of equation (2.1.4) indicates that f will be large for small mean-square displacements (in tightly bound nucleus) with small γ–ray energies and $< x^2 >$ can be determined from the vibrational properties of the crystal lattice. In the Debye model, vibrational modes of atoms follow a continous distribution in frequency up to a maximum ω_D, called the Debye frequency, which is related to the Debye temperature (θ_D) as follows:

$$\theta_D = \frac{\hbar\omega_D}{k_B}. \tag{2.1.5}$$

In the Debye approximation equation (2.1.4) reduces to

$$f = exp\left[-\frac{6E_R}{k_B\theta_D}\left[\frac{1}{4} + \left(\frac{T}{\theta_D}\right)^2 \int_0^{\theta_D/T} \frac{xdx}{e^x - 1}\right]\right] \tag{2.1.6}$$

where $x = \hbar/k_BT$. Equation (2.1.6) indicates that f is large when θ_D is large (a strong lattice), recoil energy and temperature T are low. For $T =$ 0 K,

$$f = exp\left(-\frac{3E_R}{2k_B\theta_D}\right). \tag{2.1.7}$$

The favourable conditions fo resonant absorbtion place restrictions on the nuclei suitable for Mössbauer spectroscopy. A typical Mössbauer nucleus is ^{57}Fe, which is produced by the radioactive decay of ^{57}Co is ideally suited for study of iron based compounds. Resonant absorption is easily achieved by oscillating the γ–ray source or absorber with speeds of the order of 10 mm/s.

2.2 Hyperfine interactions

The energies of the nuclear states are weakly influenced by the chemical environment of the sample. The interactions to be considered are the magnetic

and the electrostatic interactions of the nucleus with its surroundings. These together form 'hyperfine' interactions, which are reviewed in this section.

2.2.1 Isomer shift

The nucleus has a finite size which changes fractionally when it makes a transition from an excited to a ground state. Thus in general the nuclear radius is different for each nuclear energy level. This change in size during nuclear transition causes a change in Coulombic interaction between the charge of electrons at the nuclear site and the positive charge of the nucleus. This results in a shift but not splitting of nuclear energy levels called isomer (chemical or center) shift, δ. This effect is shown in Figure 2.2 (a). The expression for the isomer shift is [26]

$$\delta = \left(\frac{2\pi Ze^2}{5}\right)(|\psi_A(0)|^2 - |\psi_S(0)|^2)(R_{ex}^2 - R_{gd}^2) \qquad (2.2.1)$$

where Z is the atomic number, e is the electronic charge, $|\psi_S(0)|^2$ and $|\psi_A(0)|^2$ are s–electron densities at the nuclear sites of the source and absorber respectively, R_{ex} and R_{gd} are nuclear radii in the excited and ground states respectively. For convenience this energy shift, δ is usually quoted in mm/s rather than energy units. 1 mm/s is proportional to 4.8×10^{-8} keV for the ^{57}Fe isotope. The change in nuclear radius provides information about the s-electron density at the absorber nucleus. Equation (2.2.1) shows that if it is positive (excited state nucleus has larger size than ground state nucleus), a positive value of isomer shift indicates higher s–electron density at the absorber than at the source. For the 14.41 keV level in ^{57}Fe, the change in radius is negative because the nucleus is smaller in an excited state than in the ground state [7]. Therefore when using this Mössbauer isotope a more positive isomer shift indicates lower electron density at the absorber than at the source, and is seen as shift of the center of measured spectrum towards a positive velocity. Since the change in the nuclear radius is constant for a particular Mössbauer transition,

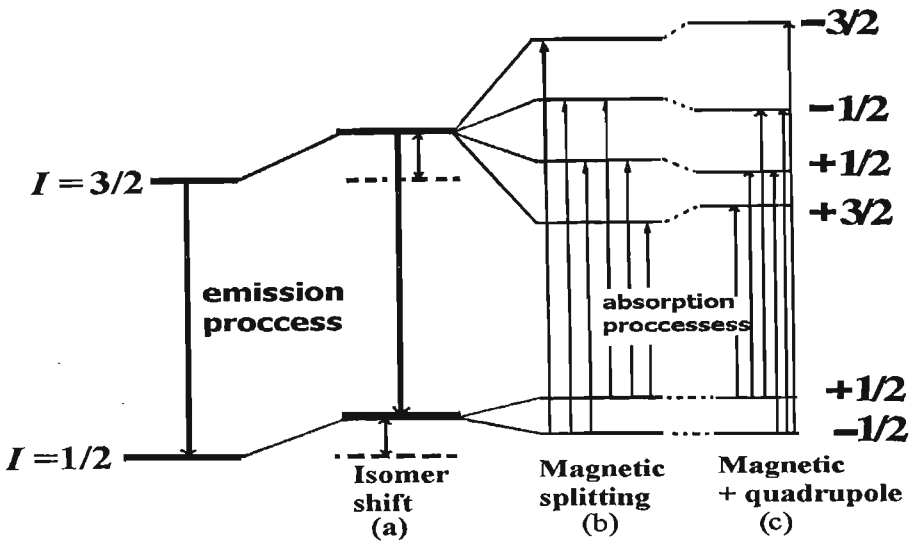

Figure 2.2: (a) Isomer shift, (b) Magnetic splitting and (c) Splitting due to combined magnetic and quadrupole splitting of the $3/2 \longrightarrow 1/2$ transition in ^{57}Fe.

equation (2.2.1) can be written as

$$\delta = K(|\psi_A(0)|^2 - |\psi_S(0)|^2) \tag{2.2.2}$$

where K is a constant depending on the change in nuclear radius. In a Mössbauer experiment the isomer shift is measured independently of the nature of the source. This is achieved by adapting the centroid of a metallic iron foil spectrum, measured at room temperature, as the reference and all energy shifts are measured relative to it and equation (2.2.2) reduces to [25]

$$\delta = K_0 - K|\psi_A(0)|^2 \tag{2.2.3}$$

where K_0 is a constant. The isomer shift is clearly a direct function of the s electron density at the nuclear site of the absorber. It is therefore sensitive to changes of orbital occupation in the valence shell of the absorber atom. The isomer shift provides the means to investigate oxidation states and covalency effects. In a Fe ion, the 1s and 2s electron density at the nucleus does not

depend on the chemical environment and the outer 4s electrons are screened from the nucleus by 3d electrons. This screening effect results in lower s electron density which shows as a lower isomer shift. An electron removed from the 3d orbital during the oxidation of Fe^{2+} to Fe^{3+} causes a decrease of the screening effect resulting in higher electron density for Fe^{3+} compared to Fe^{2+}. This gives a more negative isomer shift for Fe^{3+} than Fe^{2+} [25]. Therefore each oxidation state has different isomer shift. However, different compounds within the same oxidation state can have different isomer shifts. This is attributed to different spin states with different screening effects. Fe^{2+} can be in low, intermediate or high spin states. These states show different isomer shifts. A higher degree of covalent bonding is associated with a low isomer shift because a high covalent character reduces screening the effects [2].

2.2.2 Electric quadrupole interactions

The interaction between the local electric field gradient $\nabla\vec{E}$ produced by the electronic charges in a crystal and nuclear quadrupole moment, $\vec{Q}$, also results in the splitting of nuclear energy levels. This electric quadrupole interaction is described by the Hamiltonian

$$H = -\frac{e}{6}\vec{Q}.\nabla\vec{E}. \tag{2.2.4}$$

The eigenvalues of H are [2]

$$E_Q = eV_{zz}Q\frac{3m_I^2 - I(I+1)}{4I(2I-1)}\sqrt{\left(1+\frac{\eta^2}{3}\right)} \tag{2.2.5}$$

where η is an asymmetry parameter and V_{zz} is the component of the electric field gradient tensor along the z axis. m_I is the magnetic quantum number of the nuclear state considered and takes $2I+1$ values of I, I-1, ..., $-I$.

For the case of ^{57}Fe, the Mössbauer transition is between the nuclear ground state with spin $I_g = 1/2$ and the first excited state with spin $I_e = 3/2$. The excited state splits into two energy levels, corresponding to $m_I = \pm 3/2$ and $m_I = \pm 1/2$ with energy $E_Q = eV_{zz}Q/4$ and $E_Q = -eV_{zz}Q/4$ respectively,

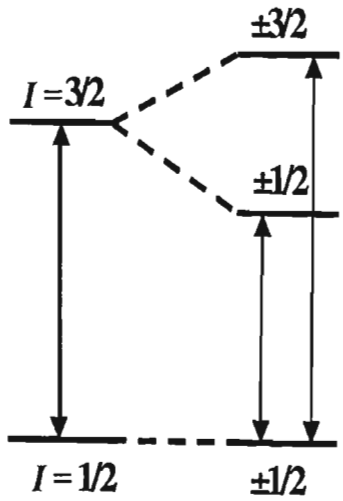

Figure 2.3: Quadrupole splitting for $3/2 \longrightarrow 1/2$ transition in ^{57}Fe.

whilst the ground state is unsplit. According to the selection rules two transitions are allowed, as illustrated in Figure 2.3. The resulting Mössbauer spectrum [2] has two absorption peaks with separation

$$\nabla = \frac{1}{2} eV_{zz}Q \tag{2.2.6}$$

called the quadrupole splitting.

2.2.3 Magnetic hyperfine interactions

The energy of a nucleus with magnetic moment $\overrightarrow{\mu}$ and spin quantum number I is perturbed by the presence of a magnetic field. This is because the nucleus has a dipole interaction with the field and this raises the degeneracy of the nuclear states by splitting the energy levels into sub-levels. In the presence of the magnetic field $\overrightarrow{B}$, the interaction energy is [2]

$$H = -\overrightarrow{\mu}.\overrightarrow{B} = -g\mu_N \overrightarrow{I}.\overrightarrow{B} \tag{2.2.7}$$

where μ_N is the nuclear magneton and g is the nuclear g-factor. The eigenvalues of the above equation are

$$E_m = -\frac{\mu B}{I} m_I = -g\mu_N B m_I \tag{2.2.8}$$

where m_I is the magnetic quantum number and takes values $I, I-1, \ldots, -I$. This means that the magnetic field splits the energy levels into $(2I+1)$ non-degenerate equi-spaced sub-levels with the energy separation $\mu B/I$. The magnetic field is the combination of the applied and the hyperfine fields.

In Mössbauer experiments both the ground and the excited states split according to equation (2.2.8) in the presence of a magnetic field. This splitting is also known as Zeeman splitting. The transitions between any two energy levels take place provided that the selection rules $\nabla m_I = 0$ or ± 1 are satisfied. The magnetic hyperfine splitting of the energy levels in ^{57}Fe nucleus is illustrated in Figure 2.2 (b). For this isotope the ground state $I = 1/2$ splits into two, and the excited state $I = 3/2$ splits into four energy levels. The six lines observed are the allowed transitions.

2.2.4 Combined magnetic and quadrupole interaction

If the nucleus with magnetic moment $\vec{\mu}$ and spin I experiences both the electric field gradient and the magnetic field simultaneously, both quadrupole and magnetic splitting of nuclear energy levels occur. The Hamiltonian describing this effect is given by the sum of equations (2.2.4) and (2.2.7). Treating quadrupole interaction as a perturbation upon magnetic interaction, the energy levels for the $1/2 \longrightarrow 3/2$ transition are given by [2]

$$E_{QM} = \frac{e^2qQ}{4}\left((-1)^{|m_z|+1/2}\right)\left(\frac{3cos^2\theta - 1}{2}\right) - g\mu_N \vec{I}.\vec{B} \tag{2.2.9}$$

where θ is the angle between the magnetic axis and the major axis of the electric field gradient tensor. In addition to magnetic splitting the energy levels are displaced by a quantity

$$\frac{e^2qQ}{4}\left(\frac{3cos^2\theta - 1}{2}\right). \tag{2.2.10}$$

This is illustrated in Figure 2.2 (c) for a Mössbauer transition in ^{57}Fe. The resulting Mössbauer spectrum has six lines but is not symmetrical about the centroid [2].

In the following chapter a discussion of the experimental techniques and procedures employed in this work is presented.

Chapter 3

Experimental techniques

3.1 Sample preparation

Several reports have appeared in the literature [3, 5, 8, 16–24] which show that ferrites are commonly produced by solid state reaction. This technique is also used extensively in industry [20] and is commonly known as the double sintering ceramic method. This is because samples are sintered twice at high temperatures. Sometimes the samples are heat treated in sealed quartz tubes and degassed under vacuum so that pellets can be quenched into liquid nitrogen immediately after the heat treatment. This helps to preserve the phase of the sample that occurs at high temperature.

Wet chemical methods like co-precipitation [6, 15] and sol–gel [9] are also used. In the co–precipitation technique, required proportions of nitrates or chlorides are mixed. Carbonates are precipitated out of the solution by adding ammonium carbonate. The clean precipitates are then heat treated at high temperature to drive off carbon as carbon monoxide. The resulting compounds are pressed into pellets and refired at higher temperature. In the sol–gel method nitrates are used as starting materials. The nitrate solution is dehydrated to form a gel. The gel is heat treated at different temperatures until fine powdered samples are formed.

In the current work, the solid state reaction method was used. High purity

oxides supplied by Aldrich Chemical Company were used as starting materials. The purity of the oxides were as follows: CdO (99 %), ZnO (99.99 %), TiO (99.99 %), Co_3O_4 (99.999 %), Fe_2O_3 (99.995 %) and Al_2O_4 (99.98 %). The starting oxides were weighed using an electronic balance in the required proportions. The total mass of each oxide mixture was about 1 gram. The mixtures were ground to fine powder in methanol using an agate mortar and pestle for about 40 minutes. Grinding was carried under a 100 W study lamp. This is helpful in the drying process of the mixture. Dry powders of samples were then pressed in a stainless steel die (12 mm in diameter) under pressure of about 2 tons/cm^2 applied for 2 minutes to form pellets. A complete set of pellets for a given system were mounted into a quartz tube open on both ends and put in the furnace as shown in Figure 3.1. This arrangement has the advantage of allowing gas flow over the entire surface of each pellet. The pellets were pre-sintered at 950 °C in flowing oxygen for about 50 hours in a microprocessor controlled Carbolite furnace (type: 12/75) with maximum temperature of 1200 °C. After this heat treatment each pellet was crushed and reground to fine powder. This dry grinding was done under aluminum foil cover to minimize mass loss while breaking and grinding pellets. The resulting fine powders were again pressed to form a second set of pellets which were finally sintered for another 50 hours at 1050 °C and 1100 °C for (Cd, Zn)$_x$Co$_{1-x}$Fe$_{2-x}$Al$_x$O$_4$ and (Cd, Zn)$_x$Co$_{0.9}$Fe$_{1.7-x}$Ti$_{0.4}$O$_4$ compounds respectively.

Figure 3.2 shows a typical variation of the sample mass during the preparation process for Cd and Al based samples. A relatively large drop in sample mass (about 5.8 %) is observed after the first heat treatment. This is mainly attributed to evaporation of some residue methanol and loss of excess oxygen during heat treatment. The mass loss after the first grinding process occurs due to some sample sticking to the agate mortar and pestle. The average mass loss during this step was about 2.2 %. A mass loss of about 0.8 % occured as the samples were pressed to make the first set of pellets. This is attributed to some mass loss in the die. This loss can be reduced by ensuring well dried samples

Figure 3.1: Schematic representation of the quartz tube with a set of pellets in the furnace.

before pressing. The average mass losses after grinding, pre–sintering, second pressing and final-sintering at 1100 ^{o}C were about 0.4 %, 0.1 % and 0.4 %, respectively. The mass of a pellet at the end of the sintering process was about 0.95 g and its typical thickness and diameter obtained, using a micrometer, were approximately 2.00 mm and 12.00 mm respectively.

3.2 Mössbauer spectroscopy

In Mössbauer spectroscopy, γ–rays emitted by nuclei from a radioactive source can be absorbed by identical nuclei in an absorber if the resonant condition is satisfied. The ideal radioactive source used in the study of iron based systems is ^{57}Co. In this work, a 10 mCi ^{57}Co source sealed in rhodium matrix was used. The decay scheme of the source is shown in Figure 3.3 [7]. ^{57}Co nuclei decay into ^{57}Fe nuclei in the excited state through the process of electron capture (EC). The 14.41 keV energy peak is utilized in Mössbauer experiments. Resonant absorption therefore depends on the amount of ^{57}Fe isotope present in an absorber. Since natural iron has about 2.19 % of ^{57}Fe isotope [7], the absorption spectrum takes a long time to accumulate. For the present investigation shorter measurement times are possible by using ^{57}Fe enriched iron oxide in the production of the samples. Unfortunately this was not possible because ^{57}Fe enriched iron oxide is very expensive.

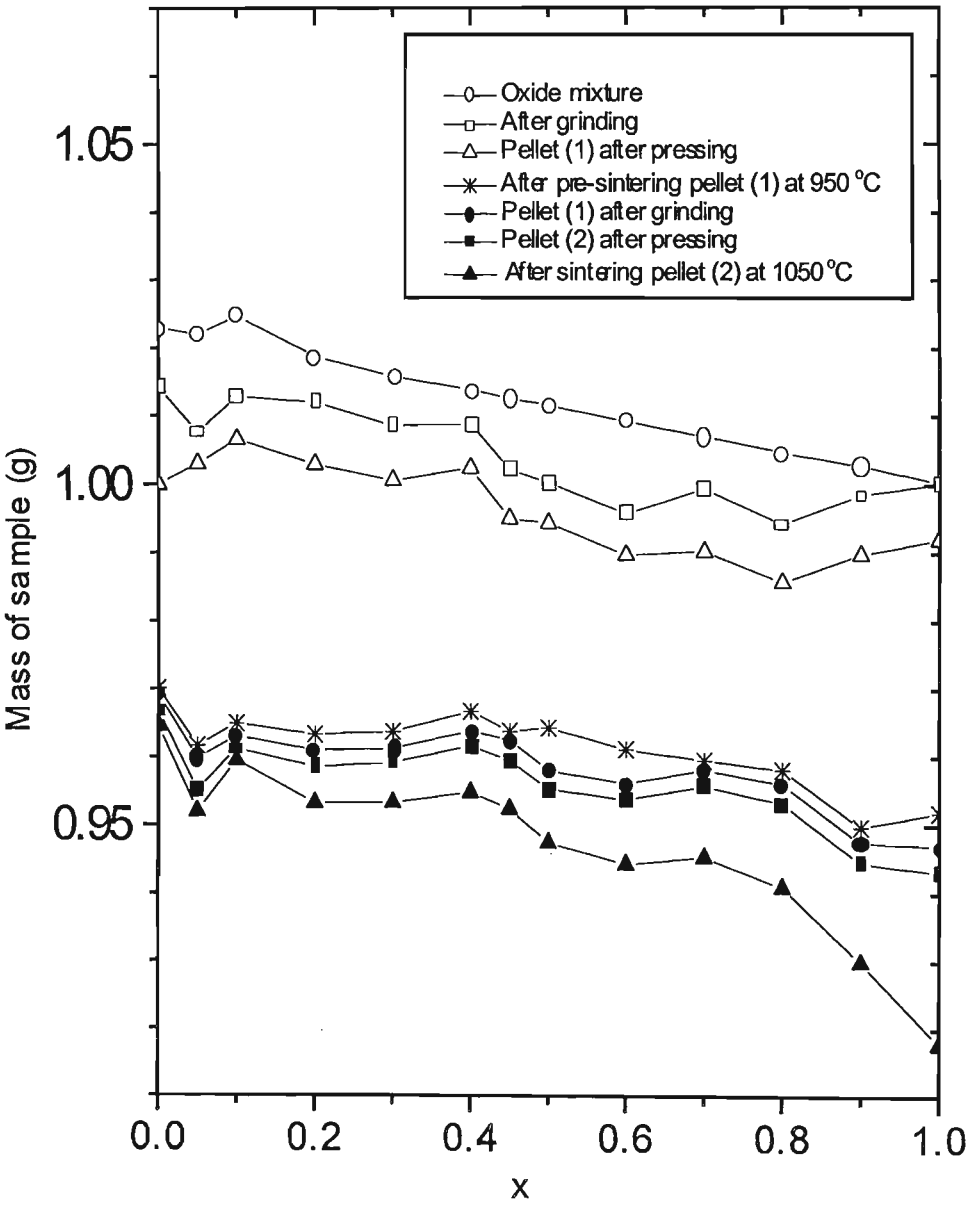

Figure 3.2: Mass reduction during preparation of $Cd_xCo_{1-x}Fe_{2-x}Al_xO_4$ samples.

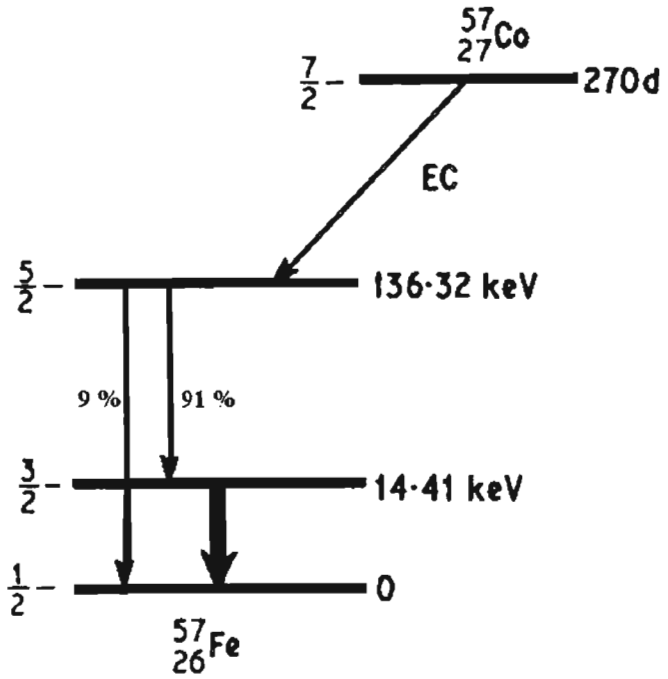

Figure 3.3: The nuclear decay scheme of ^{57}Co [7].

In the present set–up, the source was mounted to a velocity transducer which was operated at a frequency of 6 Hz and oscillated at constant acceleration. The electromechanical drive system consists of the Mössbauer driving unit (MDU) model MR–350, function generator (FG) model FG–351 and a multi channel scaling PCA3 card (supplied by Oxford Instruments) mounted in a computer. The output of the function generator have a sinusoidal or triangular wave form and repeats itself at a frequency which is proportional to the frequency of channel stepping in the card. This signal is fed to the MDU (which is a difference amplifier) where the required velocity range is selected. If a triangular wave is set as a reference signal, constantly accelerated motion of the source is produced. The drive coil in the transducer produces a voltage signal proportional to the velocity of the transducer. This signal is fed back to the MDU by a feed–back coil. The MDU compares the command signal and the feed–back signal and provides a correction to the drive coil such that the motion of the source is proportional to the signal from the function genera-

tor (which is in turn proportional to the frequency of channel stepping in the card). The source thus executes an accurate periodic motion with frequency of channel stepping in the PCA3 card. In this way the function generator is synchronized with the acceleration of the source and sweep of the memory registers in the PCA3 card, causing the open (active) channel address to be a linear function of source velocity. Thus pulses counted while the source is at a particular velocity are always stored in a particular channel. Each channel is held open for a short time interval and any counts registered by the detection system during that time interval are added to the accumulated total already stored in that channel. This results in many pulses being detected and stored in particular channels during each cycle of motion. Successive sweeps over a long period of time allow the spectrum to build up as a whole.

About 0.2 g of fine powder from each pellet was used as an absorber. The detection system was placed behind the absorber and comprised of the detector plus power supply, a pre–amplifier (Tennelec, TC174) and a main amplifier (Tennelec, TC202BLR). The detectors used were Xe,CO_2 (tube type: 4546, operational voltage 2176 V) and Kr,CO_2 (tube type: 45431, operational voltage 1789 V) gas filled proportional counters (from LND,INC., USA). The gas filled counters are commonly used in ^{57}Fe Mössbauer spectroscopy because of their good energy resolution and high signal to noise ratio for the 14.41 keV γ–rays. The detected γ–photons ionize the gas in the detector. The ejected electrons are attracted to the positive electrode. An output voltage or pulse proportional to the charge originating from ionizing events, and consequently proportional to the deposited energy, is generated by the charge sensitive amplifier. These output voltage pulses are directed via the linear amplifier to the PCA3 card. The γ–ray photons detected are those that are transmitted through the absorber. The Mössbauer spectrum thus shows low counts at certain velocities (energies) corresponding to photons which are resonantly absorbed. The 14.41 keV energy level has a mean lifetime of 1.4×10^{-7} s and a line width of $\Gamma = 4.6 \times 10^{-9}$ eV (proportional to 0.096 mm/s [25]). The absorption

spectrum is therefore expected to be a single Lorentzian of width 0.192 mm/s at half maximum centered at zero velocity. However, this is complicated by the presence of hyperfine interactions at the ^{57}Fe nuclei.

The Mössbauer spectrum of a 25 μm thick iron absorber measured at room temperature is shown in Figure 3.4. This iron foil was used for velocity calibration of the spectra. The values of the zero velocity channel (ZVC) and calibration factors (CF) measured from time to time by the MR351 or MR350/FG351 spectrometers are shown in table 3.1. Apart from providing up to date calibration parameters, this was helpful in monitoring the performance of the spectrometers. The CF and ZVC values are found to be constant for the same velocity range for a given spectrometer.

The layout of each Mössbauer spectrometer used is shown in Figure 3.5. The multi channel scaling PCA3 card was used for data acquisition instead of a multi–channel analyzer (MCA) traditionally used in Mössbauer spectroscopy. The advantage of a PCA3 card is the combination of lower cost and easier way of storage and access of data for further analysis. Initially the card is connected in pulse height analysis (PHA) mode in order to select the 14.41 keV Mössbauer peak. During the PHA mode the connections SCA to MCS/REJ, CHA to BSY/DWLL and START/ADD to EXTSY shown in Figure 3.5 are disconnected. The Mössbauer peak was selected by adjusting the two outer screws at the back of the card. When using the function generator FG–351, the spectrometer was connected as shown in Figure 3.5 in MCS mode of operation. To initiate data acquisition the following steps were followed:

- The computer was started and PCA3 directory entered. The command line: PCA3 O h n ('O' switch updates display, 'h' switch keeps software resident when exiting program and 'n' switch removes title screen) was entered.

- The PCA3 screen was now present. Ctrl+F2 was pressed to clear the screen from any random bits of data.

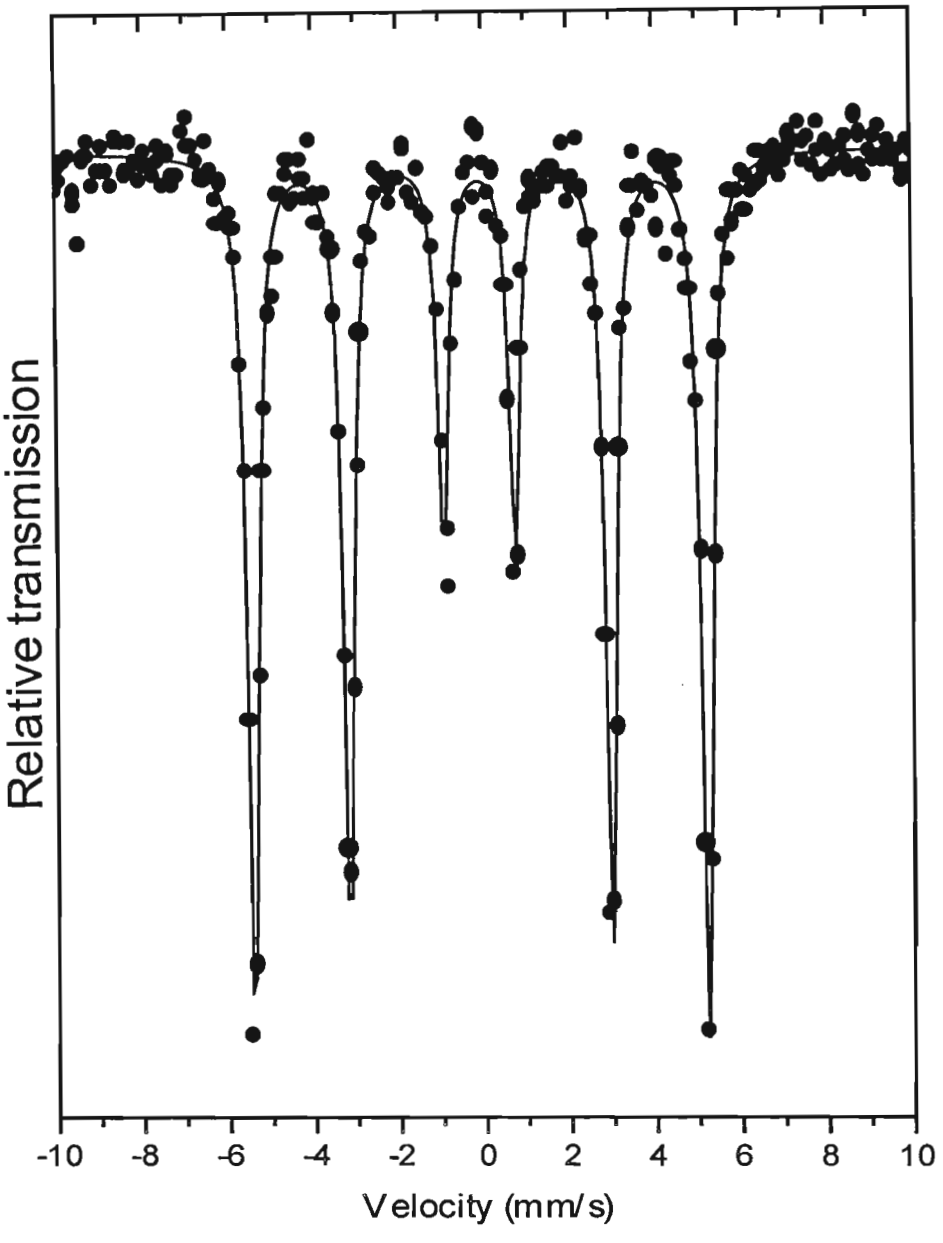

Figure 3.4: ^{57}Fe Mössbauer spectrum of a metallic ion foil, measured at room temperature.

Table 3.1: Calibration factor (CF) and zero velocity channel (ZVC) measured at different times and velocity ranges (VR).

Date	Spectrometer	VR (mm/s)	CF (mm/s)	ZVC (mm/s)
23/11/2000	MR351	10	0.1094	129.02
05/12/2000	MR351	10	0.1095	129.02
26/12/2000	MR351	10	0.1095	129.02
08/01/2001	MR351	10	0.1094	129.02
18/12/2000	MR351	3	0.0330	129.09
21/12/2000	MR351	3	0.0330	129.04
25/01/2001	MR351	3	0.0330	128.98
28/02/2001	MR350/FG351	15	0.1049	129.05
14/03/2001	MR350/FG351	15	0.1044	128.55
10/09/2001	MR350/FG351	15	0.1037	129.03
12/09/2001	MR350/FG351	15	0.1037	129.03
06/04/2001	MR350/FG351	12	0.0829	129.04
23/05/2001	MR350/FG351	12	0.0821	129.05
15/02/2001	MR350/FG351	10	0.0692	129.04
16/08/2001	MR350/FG351	3	0.0330	129.06
06/02/2001	MR350/FG351	2.5	0.0176	128.81
11/05/2001	MR350/FG351	2.5	0.0172	128.40
14/05/2001	MR350/FG351	2.5	0.0174	129.00

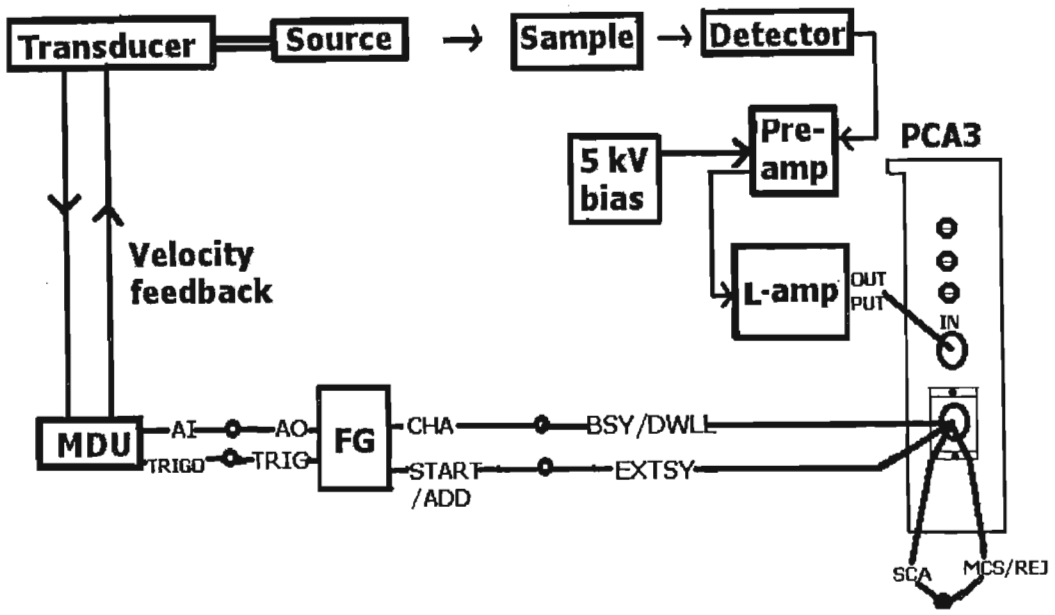

Figure 3.5: Schematic diagram of Mössbauer spectrometer used in the present experiment.

- Right mouse click (RMC) to get the arrow and left mouse click (LMC) on MODE along the top screen.
- LMC on MCS, click on DWELL and on EXTERNAL. Select division 1 and press ESC key to get rid of the MODE windows. Run the mouse arrow over SETUP.
- Use mouse to highlight MEMORY GROUP. Click on 32nd to get 512 channels. This group must match the number of channels selected on the FG–351 channel selector switch. A smaller window appears, and for now just click on division 1.
- Set the vertical scale by pressing the up and down arrows. Select the range you want and press ENTER.
- The data will go from the amplifier to the PHA connector on the back of the PCA3 card.

- The Mössbauer spectrometer was started and once it was running smoothly, F1 key on the keyboard was pressed to initiate the MCS acquisition on the PCA3. If all the cables are correctly connected and everything is set–up and turned on, you should be able to see counts in the passes block and the start of baseline rising from the bottom of the screen.

- If an iron calibration sample foil is mounted, a six line Mössbauer spectrum develops after a few minutes.

The analysis of spectra was carried out using Mosswinn 3.0i [29] and Recoil [30] Mössbauer software packages. Both software packages generate a detailed report of the fitted parameters to the data. All the Mössbauer fits presented in this work were generated by Recoil software, which was easier to use and provided better fits to the data.

3.3 X–ray diffraction

X–rays have wavelengths in the range comparable to interatomic spacing. This makes the use of x–rays ideally suited for the study of the structure of materials. X–ray diffraction (XRD) is based on the Bragg reflection of x–rays by atoms in a crystal. The incident beam is passed through a special filter in order to obtain a monochromatic beam of wavelength λ. This radiation is diffracted by a crystal when the condition for Bragg reflection

$$n\lambda = 2d\sin\theta \tag{3.3.1}$$

is satisfied. n is an integer and d is the spacing of the planes of atoms in a crystal. The Bragg angle θ is the glancing angle at which the x–ray beam strikes the crystal. In the powder diffraction method, a powdered sample is rotated in the beam. Each particle in the powder acts as a crystal mounted at random with respect to the beam. As the sample is rotated different planes at different Bragg angles diffract. Diffraction takes place from those planes of particles

oriented such that Bragg equation (3.3.1) is satisfied. The spectrum therefore consists of different diffraction lines at different 2θ values. Equation (3.3.1) indicates that if an x–ray beam of known wavelength λ is used, the spacing of the planes of atoms (d) can be calculated. Since in ferrites the spinel structure is cubic, d is related to the size of the unit cell lattice parameter a by [27]

$$a = d(h^2 + k^2 + l^2)^{\frac{1}{2}} \tag{3.3.2}$$

where (hkl) are Miller indices. Equation (3.3.1) and (3.3.2) give

$$n\lambda = 2a(h^2 + k^2 + l^2)^{\frac{1}{2}} \sin\theta. \tag{3.3.3}$$

Equation (3.3.3) indicates that to determine lattice constant a we only need to assign correct Miller indices to each diffraction line.

In the present work, powder XRD was used to characterize the samples. The measurements were carried out in the School of Geological and Computer Sciences at the University of Natal using a Phillips diffractometer type PW1710. A monochromatic beam of Co (K_α) radiation of wavelength $\lambda = 1.78897$ $\mathring{A}$ was used in the measurements. About 0.4 g of fine powder of each pellet was mounted in the x–ray diffractometer. The nature, size of the unit cell and quality of the samples were determined from the diffraction patterns. In addition, information about the density, porosity and grain sizes were also obtained.

Chapter 4

The $(Cd, Zn)_xCo_{0.9}Fe_{1.7-x}Ti_{0.4}O_4$ spinel system

4.1 Introduction

In this chapter the X–ray and the Mössbauer results for $(Zn, Cd)_xCo_{0.9}Fe_{1.7-x}Ti_{0.4}O_4$ spinel oxides prepared by using a standard ceramic process (discussed in section 3.1) are presented. The A site of the compound $Co_{0.9}Fe_{1.7}Ti_{0.4}O_4$ is being diluted by Cd or Zn.

4.2 X–ray diffraction results

The compositional dependence of X–ray diffractograms for Zn and Cd based samples are shown in Figures 4.1 and 4.2 respectively. Sharp X-ray diffraction lines were obtained for all samples. The most significant lines were successfully indexed using the XRD data of magnetite [32] which has a cubic spinel structure [4]. This confirms the predominance of single-phase formation in the samples. Lattice parameters, densities, porosity and grain sizes data derived from XRD patterns are presented in the following sections.

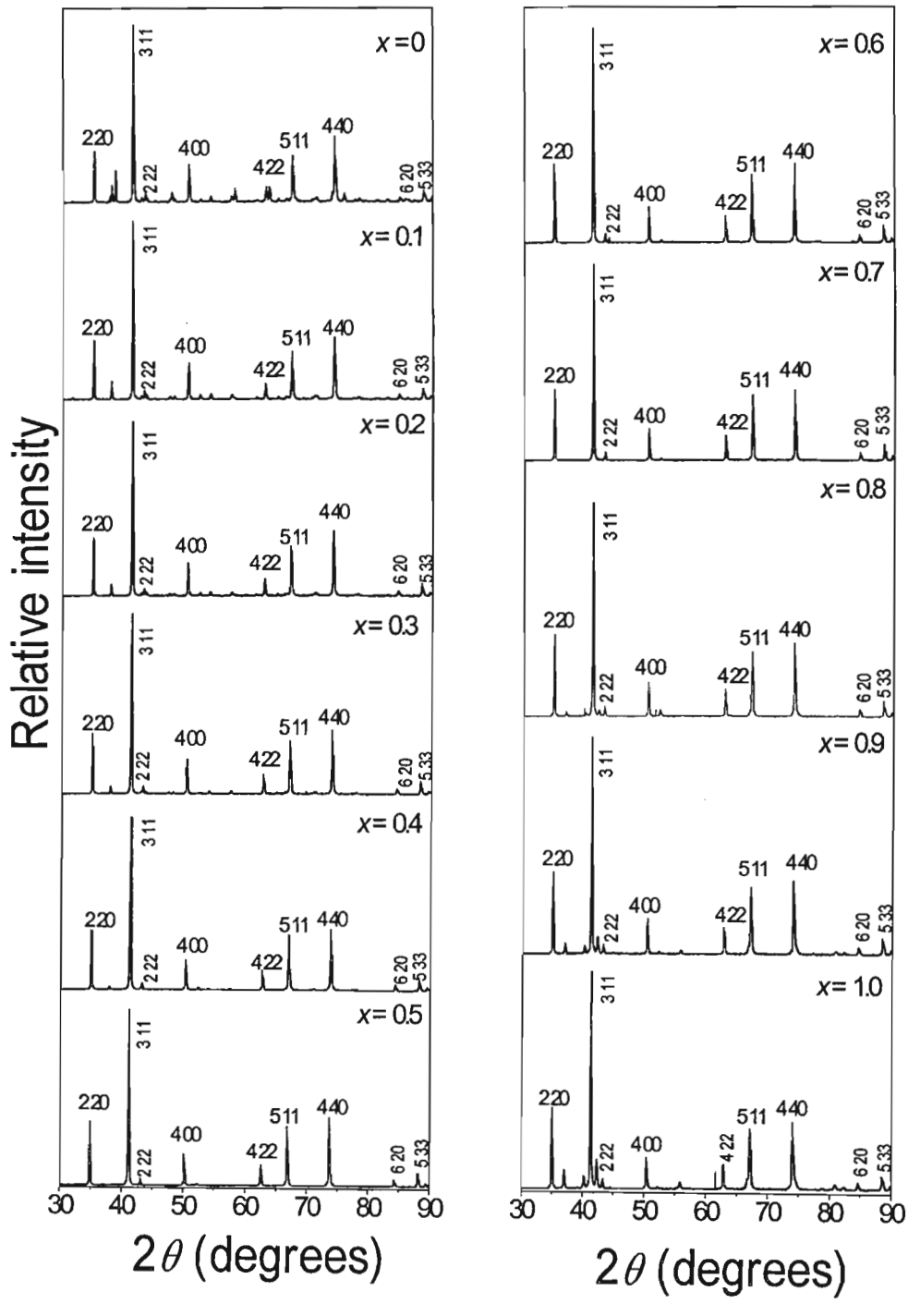

Figure 4.1: X–ray diffraction patterns for $Zn_xCo_{0.9}Fe_{1.7-x}Ti_{0.4}O_4$.

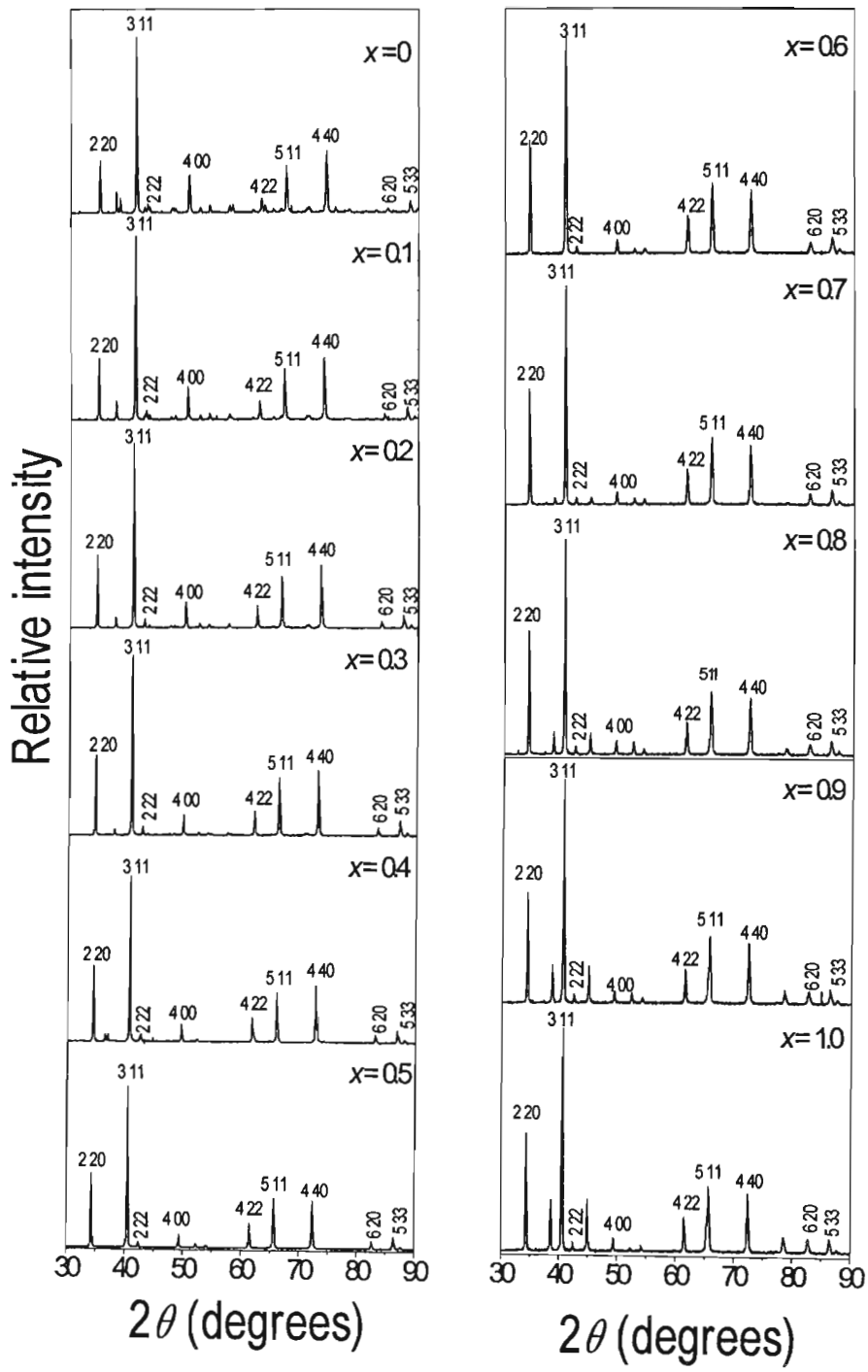

Figure 4.2: X–ray diffraction patterns for $Cd_xCo_{0.9}Fe_{1.7-x}Ti_{0.4}O_4$.

4.2.1 Lattice parameters

The values of the lattice parameter a of the Zn and Cd based spinel oxides are respectively shown in tables 4.1 and 4.2 and plotted against x in Figure 4.3. The lattice parameters were calculated using equation (3.3.2). The data changes linearly with x, obeying Vergad's law [19]. The values compare well with the previously reported values [12, 16, 21, 23] of similar compounds. Cd substituted compounds show an increase in a with x up to $x = 0.7$. A decrease is observed with further substitution by Cd. In Zn compounds, a increases with x up to a maximum value at $x = 0.5$ and then decreases with x. The increase and decrease in a respectively indicate an expansion and a contraction of the unit cell. The change in size of a unit cell with x can be explained on the basis of the changes in the distances between the A or B site cations and the oxygen anions due to size difference of cations involved. The shortest distances between oxygen ion and A site or B site cations are known as tetrahedral (R_{A}) and octahedral (R_{B}) radii respectively. They can be calculated from the distribution of cations on A and B sites. For samples with chemical formula $(\mathrm{Cd, Zn})_x\mathrm{Co}_{0.9}\mathrm{Fe}_{1.7-x}\mathrm{Ti}_{0.4}\mathrm{O}_4$ the cation distribution given by equation (1.4.1) becomes [16]

$$\left(M_x^{2+}\mathrm{Fe}_{1-x}^{3+}\right)^{\mathrm{A}}\left(\mathrm{Co}_{0.9}^{2+}\mathrm{Fe}_{0.7}^{3+}\mathrm{Ti}_{0.4}^{4+}\right)^{\mathrm{B}}\mathrm{O}_4 \tag{4.2.1}$$

where M is Zn or Cd. This formula assumes all the Zn or Cd ions to replace the Fe ions on A site. From equation (4.2.1) the tetrahedral and octahedral radii are

$$R_{\mathrm{A}} = (R_{M^{2+}} - R_{\mathrm{Fe}^{3+}})x + R_{\mathrm{Fe}^{3+}} \tag{4.2.2}$$

and

$$R_{\mathrm{B}} = \left(0.9R_{\mathrm{Co}^{2+}} + 0.7R_{\mathrm{Fe}^{3+}} + 0.4R_{\mathrm{Ti}^{4+}}\right)/2 \tag{4.2.3}$$

respectively. Using the ionic radii values given in table 4.3, the tetrahedral radii become

$$R_{\mathrm{A}}(\mathrm{Cd}) = (0.033x + 0.064)\ \mathrm{nm} \tag{4.2.4}$$

Table 4.1: Bulk ρ_b and X–ray ρ_x density, porosity P and lattice parameter a for $Zn_xCo_{0.9}Fe_{1.7-x}Ti_{0.4}O_4$.

x	ρ_b (g/cm^3)	ρ_x (g/cm^3)	P (%)	a (Å)
	± 0.03	± 0.009	± 0.2	± 0.004
0	4.06	5.201	21.9	8.388
0.1	4.21	5.209	19.2	8.396
0.2	4.39	5.215	15.6	8.404
0.3	4.55	5.223	13.0	8.411
0.4	4.40	5.243	16.1	8.412
0.5	4.29	5.252	18.3	8.418
0.6	4.10	5.286	22.4	8.412
0.7	4.36	5.327	18.1	8.401
0.8	4.58	5.353	14.5	8.398
0.9	4.27	5.378	20.5	8.397
1.0	4.36	5.415	20.3	8.389

and

$$R_A(\text{Zn}) = (0.010x + 0.064) \text{ nm}. \tag{4.2.5}$$

In both Cd and Zn based samples it is expected that $R_B = 0.0684$ nm. The variation of R_A and R_B with Cd or Zn content is shown in Figure 4.4. R_A increases with x for the whole composition range in both Cd and Zn compounds. The increase in R_A in Cd based compounds is higher than in Zn based compounds, consistent with larger size of the Cd atom compared to Zn. This increase in tetrahedral radius R_A indicates the expansion of the A site sphere which in turn gives rise to expansion of the unit cell. The expansion is expected as the smaller Fe^{3+} ions are being substituted by larger Zn^{2+} or Cd^{2+} ions (see table 4.3) on the A site. This happens for $x \leq 0.7$ and for $x \leq 0.5$ in Cd

Table 4.2: Bulk ρ_b and X–ray ρ_x density, porosity P and lattice parameter a for $Cd_xCo_{0.9}Fe_{1.7-x}Ti_{0.4}O_4$.

x	ρ_b (g/cm^3)	ρ_x (g/cm^3)	P (%)	a ($\AA$)
	$\pm$ 0.03	$\pm$ 0.009	$\pm$ 0.2	$\pm$ 0.005
0	3.26	5.180	37.1	8.400
0.1	3.80	5.244	27.8	8.433
0.2	3.85	5.294	27.3	8.473
0.3	4.08	5.350	23.7	8.508
0.4	4.07	5.442	25.2	8.524
0.5	4.33	5.486	21.1	8.564
0.6	4.18	5.580	25.1	8.577
0.7	4.31	5.687	24.2	8.583
0.8	4.35	5.813	25.1	8.580
0.9	4.38	5.960	26.5	8.566
1.0	4.51	6.091	26.0	8.561

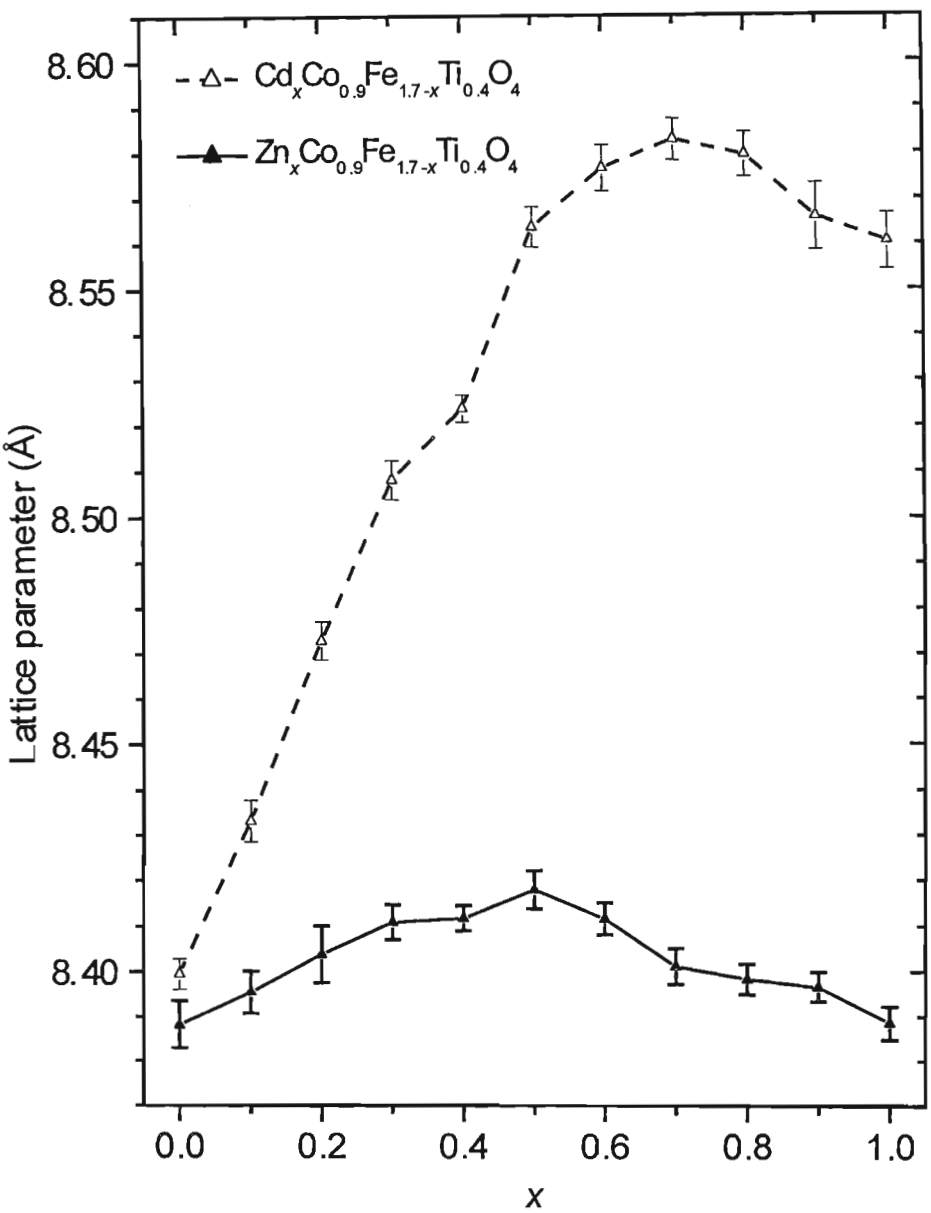

Figure 4.3: Lattice parameters for (Cd, Zn)$_x$Co$_{0.9}$Fe$_{1.7-x}$Ti$_{0.4}$O$_4$.

Table 4.3: Ionic radii values [33].

Ion	Cd^{2+}	Zn^{2+}	Co^{2+}	Al^{3+}	Ti^{4+}	Fe^{3+}
Radius (nm)	0.097	0.074	0.072	0.051	0.068	0.064

and Zn based samples respectively. A decrease in a with further substitution by Cd or Zn is observed at higher values of x. This may be due to some of the Zn or Cd ions going to B sites as well. This anomalous behavior in lattice parameters starts at higher concentration of Cd and at lower Zn concentration. This means that even though both Cd and Zn also go to a B site at high concentrations, Zn has a greater tendency. In the preliminary study by Moyo et al [17] Zn was suspected to occupy both A and B sites. This suggests a modification of the cation distribution in expression (4.2.1) to accommodate some of diamagnetic ions going to B site as well at high concentrations.

4.2.2 X–ray and bulk densities

The bulk densities were determined accurately by using geometrical methods. This was achieved by measuring the mass, diameter and thickness of each pellet after final sintering. The X–ray densities were computed from the values of lattice parameters using the formula [1, 23]

$$\rho_x = \frac{8M}{N_A a^3} \tag{4.2.6}$$

where 8 represents the number of molecules in a unit cell of the spinel lattice, M the molecular weight of the sample, a the lattice parameter, and N_A the Avogadro's number. The values of bulk and X–ray densities found in the samples are shown in tables 4.1 and 4.2 and plotted against x in Figure 4.5. These compare very well with the previously reported values [1, 23] found for a spinel structure. Both bulk and X–ray density data increase with Cd substitution. However, for Zn based compounds the bulk densities fluctuate between 4.0

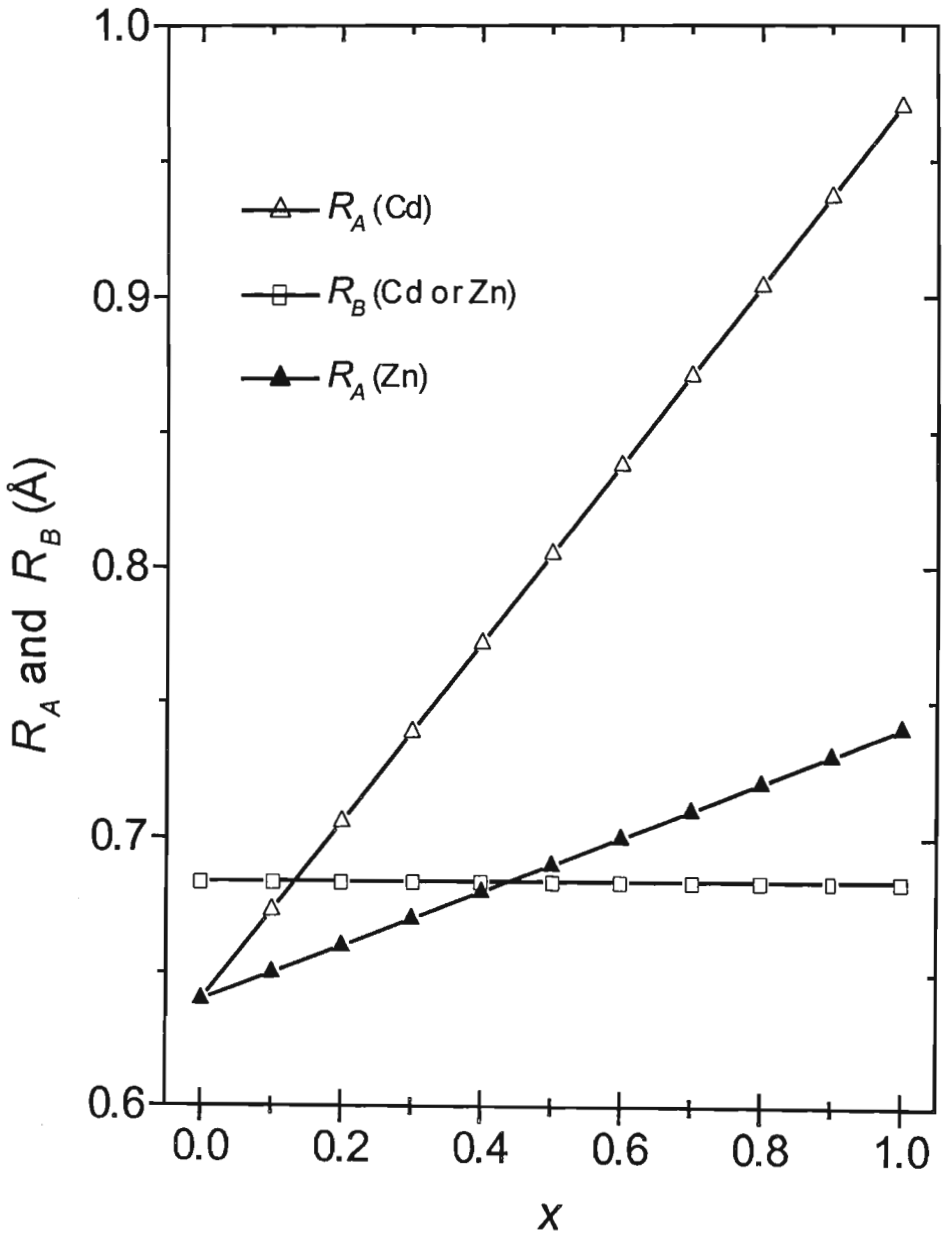

Figure 4.4: Bond lengths for (Cd, Zn)$_x$Co$_{0.9}$Fe$_{1.7-x}$Ti$_{0.4}$O$_4$.

g/cm^3 and 4.6 g/cm^3 unlike the x–ray densities which increase linearly with x. Maximum bulk densities are observed for compositions x=0.3 and 0.8. The samples found to have high densities appear to be less porous (see Figure 4.6 presented in the following section). This is expected theoretically because both porosity and density of the samples are related to the heat treatment. In both Cd and Zn based compounds the bulk densities are lower compared to the x–ray densities. This behavior was previously observed in mixed ferrites [23].

4.2.3 Porosity of samples

The percentage porosity P of the samples were deduced from the x–ray density ρ_x and bulk density ρ_b data using the formula [23]

$$P(\%) = \left(1 - \frac{\rho_b}{\rho_x}\right) \times 100. \tag{4.2.7}$$

The results of the calculations are given in tables 4.1 and 4.2. Figure 4.6 shows the composition dependence of P. The samples produced in this study are therefore highly porous, probably due to heat treatment in flowing oxygen.

4.2.4 Grain sizes of the compounds

Figure 4.7 shows the variation of grain sizes g of the compounds with x. These were calculated from the broadening of the (311) x–ray diffraction line width using the Sherrer formula [27]

$$g = \frac{K\lambda}{w_{311} cos\theta} \tag{4.2.8}$$

where K is the shape factor (taken to be 1 [27]) and w_{311} is the width of the (311) reflection line at half maximum. This reflection line occurs at about $2\theta = 41^o$ when using Co (Kα) radiation. w_{311} was calculated by fitting a Gaussian distribution on the (311) reflection line. The grain sizes fluctuated between 50 nm and 70 nm. Grain sizes in the range 10 nm to 60 nm were obtained for a $NiFe_2O_4$ ferrite after high energy ball milling [28]. The variation of the

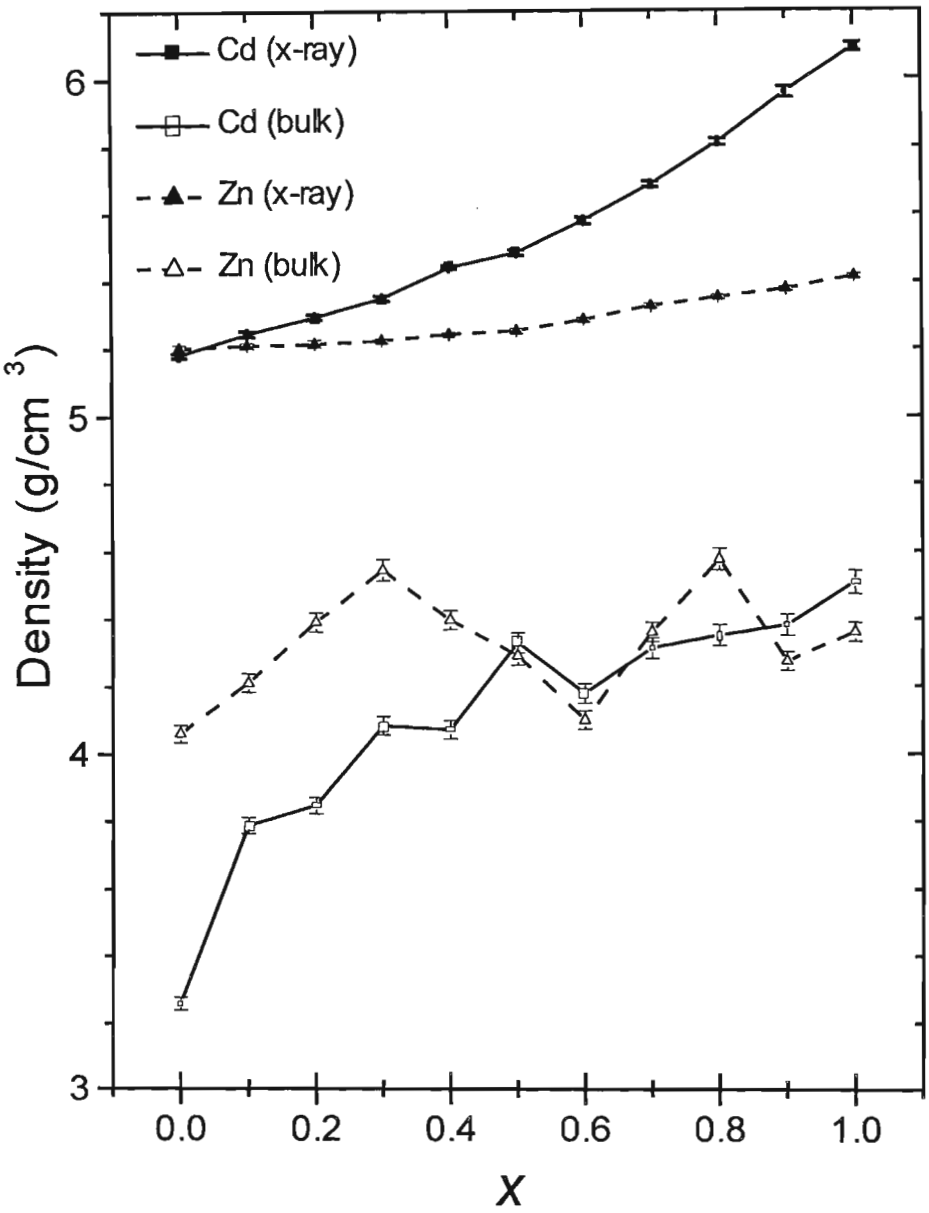

Figure 4.5: Bulk and X–ray densities for (Cd, Zn)$_x$Co$_{0.9}$Fe$_{1.7-x}$Ti$_{0.4}$O$_4$.

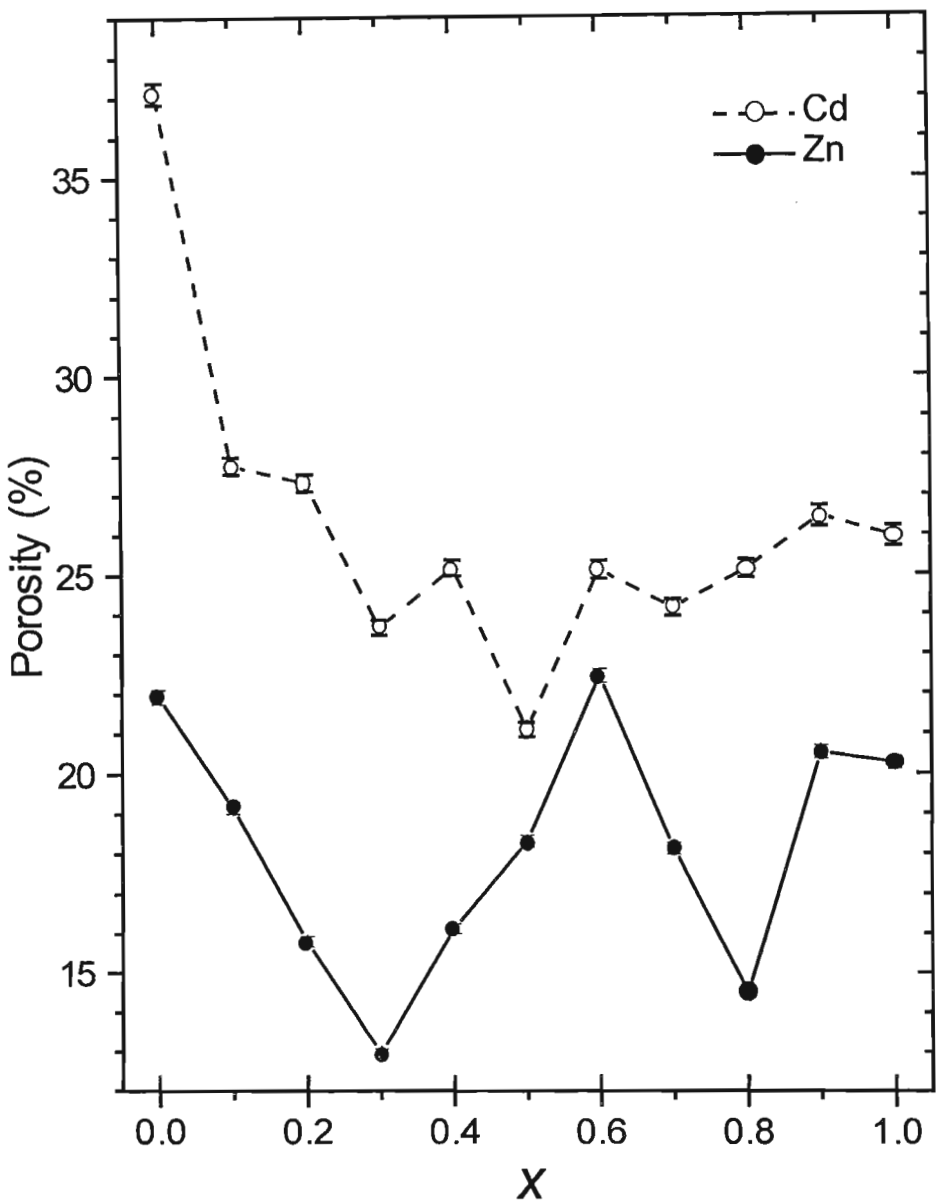

Figure 4.6: Porosity as a function of x for (Cd, Zn)$_x$Co$_{0.9}$Fe$_{1.7-x}$Ti$_{0.4}$O$_4$.

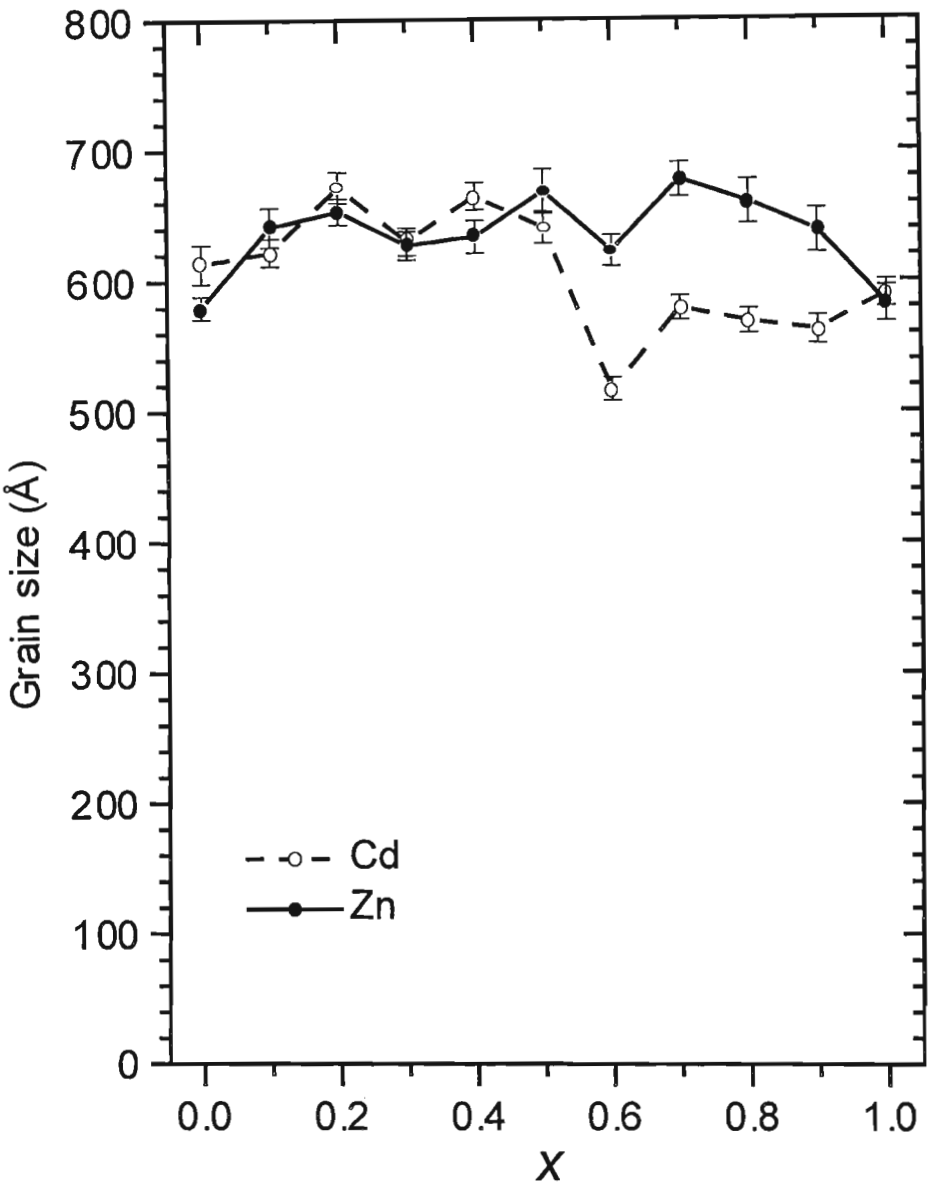

Figure 4.7: Grain sizes for (Cd, Zn)$_x$Co$_{0.9}$Fe$_{1.7-x}$Ti$_{0.4}$O$_4$.

average grain size of $NiFe_2O_4$ ferrite was found to depend on the milling time. Clearly, fluctuations in grain sizes of the samples must be due to the grinding of samples by hand using mortar and pestle and can therefore be reduced by using high energy ball milling.

4.3 Mössbauer spectroscopy results

The variation of the Mössbauer spectra with x for Zn and Cd based compounds is shown in Figures 4.8 and 4.9. These were measured at room temperature using a constant acceleration Mössbauer spectrometer discussed in section 3.2. The spectra are very closely related. This behavior is attributed to the similar electronic configuration of Cd and Zn. For $x \leq 0.4$ the spectra exhibit two normal Zeeman split sextets and a growing doublet. For $x \geq 0.5$ only symmetric doublets are observed. The magnetic split sextets reveal the ferrimagnetic behavior of the samples and the doublets reveal a paramagnetic state. For $x \leq 0.4$ the spectra were fitted with two sextets and one symmetric doublet. Each sextet corresponds to Fe ions on A or B site in an ordered spin state and the doublet corresponds to fraction of Fe ions in disordered spin state. A doublet in addition to the sextets may be due to the overlapping between A and B sites. The solid lines through the data points in Figures 4.8 and 4.9 are results of the computer fit using the Recoil Mössbauer spectral analysis software. For $x \leq 0.4$ zero quadrupole splitting was assumed for both A and B sites when fitting the sextets. Negligible quadrupole splitting has been observed by Thanki et al [8] in similar compounds. For $x \geq 0.5$ the spectra were fitted with two symmetric doublets. Each doublet represents Fe ions in a paramagnetic state on A or B site. The criterion that used to allocate sextets and doublets to A or B sites was based on fitted results of the quadrupole splitting and isomer shifts which are expected to be lower for A sites compared to B sites [1, 2, 16]. Higher quadrupole splitting on B site is due to low symmetry as discussed in section 1.1. Lower isomer shift on A site is attributed to high covalency of the

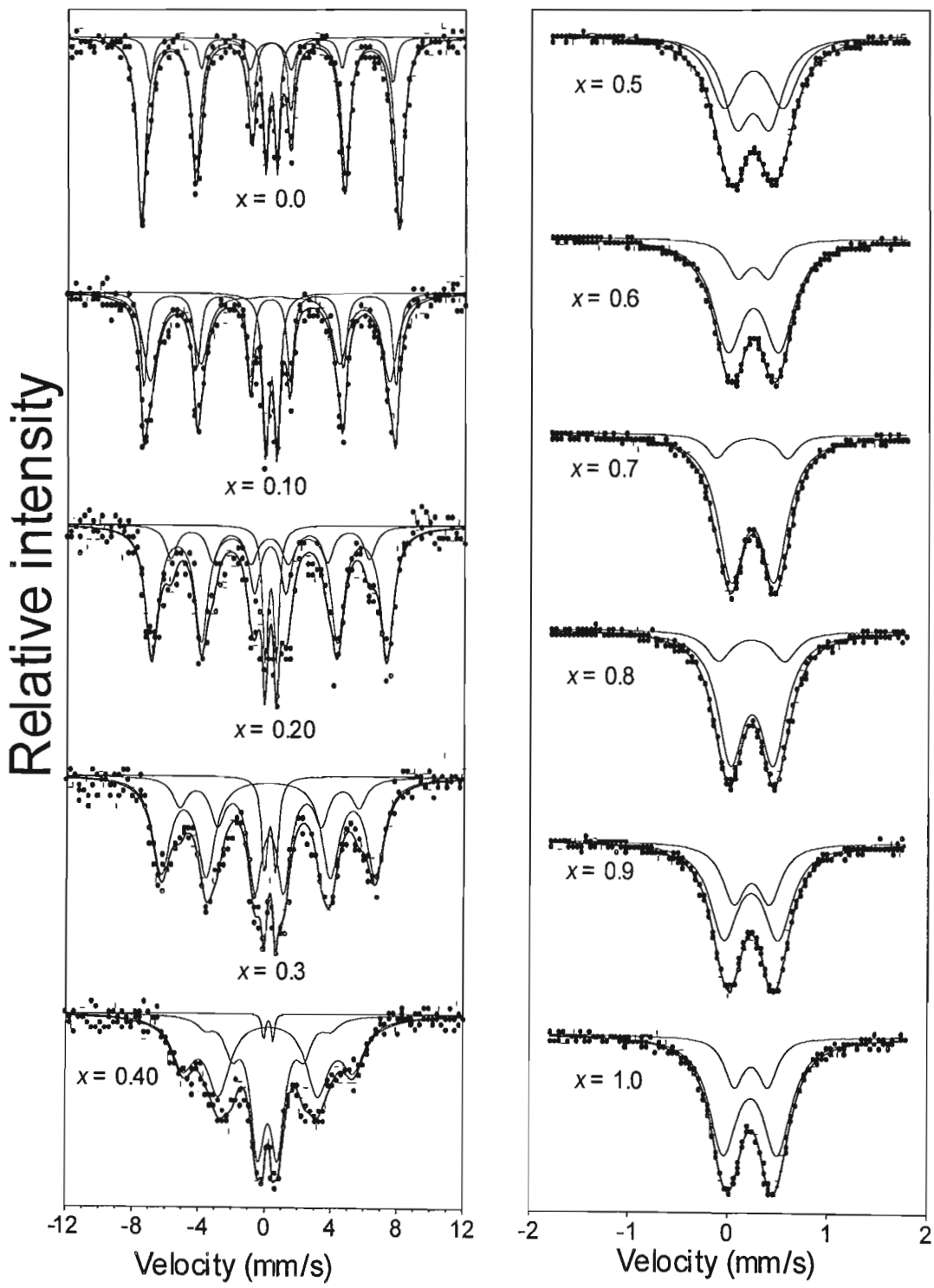

Figure 4.8: Mössbauer spectra for $Zn_xCo_{0.9}Fe_{1.7-x}Ti_{0.4}O_4$.

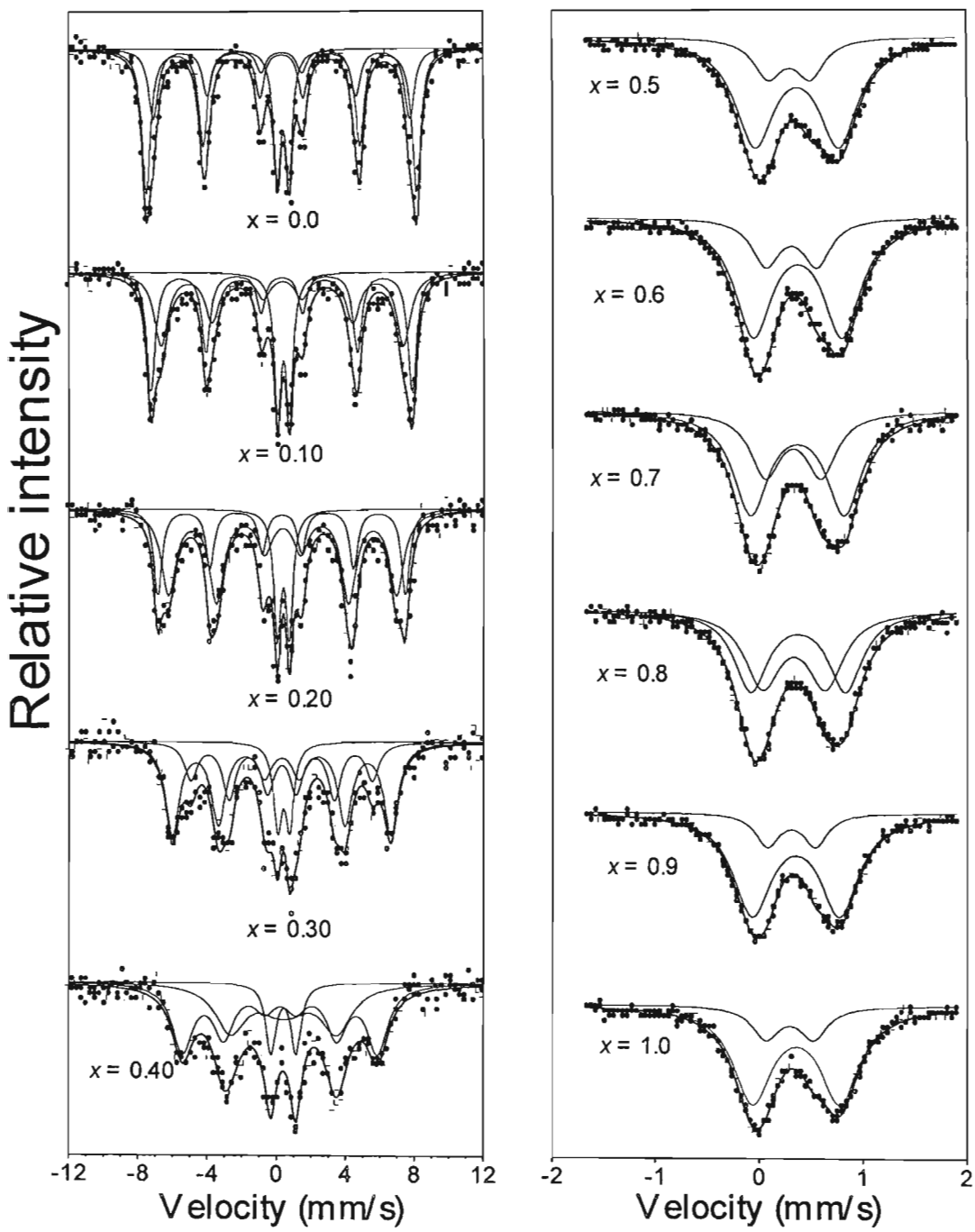

Figure 4.9: Mössbauer spectra for $Cd_xCo_{0.9}Fe_{1.7-x}Ti_{0.4}O_4$.

Fe–O bond on the tetrahedral site [1, 2].

The Mössbauer parameters for Zn and Cd based compounds are shown in tables 4.4 and 4.5 respectively. In A and B sites the isomer shifts corresponding to high spin Fe^{3+} charge state are ± 0.16 mm/s and ± 0.27 mm/s respectively [34]. The average isomer shifts values found in the present investigated samples are shown in table 4.6. These values therefore indicate the high spin Fe^{3+} charge state in the samples studied. No significant variation of isomer shift values for Fe on A and B site with x was observed. Similar behavior has been observed in similar compounds [8]. This means that diamagnetic ions are not affecting the s–electron charge distribution in Fe^{3+} ions. As expected, both quadrupole splitting and isomer shift values on A site are smaller than those on B site. These Mössbauer parameters are generally larger in Cd than in Zn based samples. This behavior is consistent with the shorter iron oxygen bond length (see Figure 4.4) predicted by the general cation distribution (4.1.1). Smaller isomer shift, quadrupole splitting, and shorter bond length reveal a high degree of covalency. High covalency in $ZnFe_2O_4$ than in $CdFe_2O_4$ ferrites was reported by Gibbs [2]. High quadrupole splitting on B than A site is due to low symmetry on B site as discussed in section (1.1). The compositional dependence of the hyperfine fields is illustrated in Figure 4.10. A systematic decrease of the hyperfine fields acting on A and B sites in the ^{57}Fe nuclei with x indicates the weakening of the magnetic coupling. This is expected because the magnetic coupling depends on the number of magnetic neighbors in the ^{57}Fe nucleus. Zn or Cd replaces the Fe^{3+} and this influences the internal hyperfine fields at the nearest Fe^{3+} site through super transferred hyperfine fields.

The variation of the fraction of Fe ions on A or B sites with x is shown in Figure 4.11. The Fe fraction is proportional to the area of a sextet or a doublet in the Mössbauer spectra. The areas are proportional to the amount of Fe ions on A or B site. These areas can therefore give information about the occupation of the interstitial sites by Zn or Cd ions. If all the diamagnetic Cd or Zn atoms were going to A site as predicted by equation (4.1.1), a decrease of

Table 4.4: Isomer shift (IS), quadrupole splitting (QS) and hyperfine fields (H) of $Zn_xCo_{0.9}Fe_{1.7-x}Ti_{0.4}O_4$.

	IS (mm/s)		QS (mm/s)		H (kOe)	
x	$(IS)_A$	$(IS)_B$	$(QS)_A$	$(QS)_B$	$(H)_A$	$(H)_B$
	± 0.03	± 0.03	± 0.02	±0.06	±8	±2
0	0.19	0.26			485	455
0.1	0.18	0.19			474	450
0.2	0.18	0.22			442	373
0.3	0.18	0.24			402	336
0.4	0.19	0.23			320	234
0.5	0.25	0.26	0.35	0.60		
0.6	0.25	0.26	0.40	0.61		
0.7	0.25	0.24	0.43	0.71		
0.8	0.25	0.25	0.43	0.66		
0.9	0.25	0.25	0.36	0.54		
1.0	0.25	0.25	0.34	0.54		

Table 4.5: Isomer shift (IS), quadrupole splitting (QS) and hyperfine fields (H) of $Cd_xCo_{0.9}Fe_{1.7-x}Ti_{0.4}O_4$.

	IS (mm/s)		QS (mm/s)		H (kOe)	
x	$(IS)_A$	$(IS)_B$	$(QS)_A$	$(QS)_B$	$(H)_A$	$(H)_B$
	± 0.04	± 0.04	± 0.04	±0.03	±2	±1
0	0.30	0.31			486	460
0.1	0.29	0.33			469	436
0.2	0.29	0.34			445	409
0.3	0.30	0.30			392	326
0.4	0.25	0.30			351	224
0.5	0.29	0.36	0.40	0.80		
0.6	0.31	0.37	0.49	0.85		
0.7	0.32	0.36	0.54	0.90		
0.8	0.33	0.37	0.61	0.91		
0.9	0.31	0.35	0.46	0.84		
1.0	0.29	0.36	0.46	0.84		

Table 4.6: Average values of isomer shifts (IS) and quadrupole splitting (QS) of sextets or doublets of $(Cd, Zn)_xCo_{0.9}Fe_{1.7-x}Ti_{0.4}O_4$.

	Zn based spinel		Cd based spinel	
Parameter	(mm/s)	x	(mm/s)	x
$< IS >_A$	0.22±0.03	(0.0<x<1.0)	0.30±0.03	(0.0<x<1.0)
$< IS >_B$	0.23±0.03	(0.0<x<1.0)	0.34±0.04	(0.0<x<1.0)
$< QS >_A$	0.38±0.03	($x\geq$ 0.5)	0.49±0.05	($x\geq$0.5)
$< QS >_B$	0.61±0.03	($x\geq$0.5)	0.86±0.03	($x\geq$0.5)

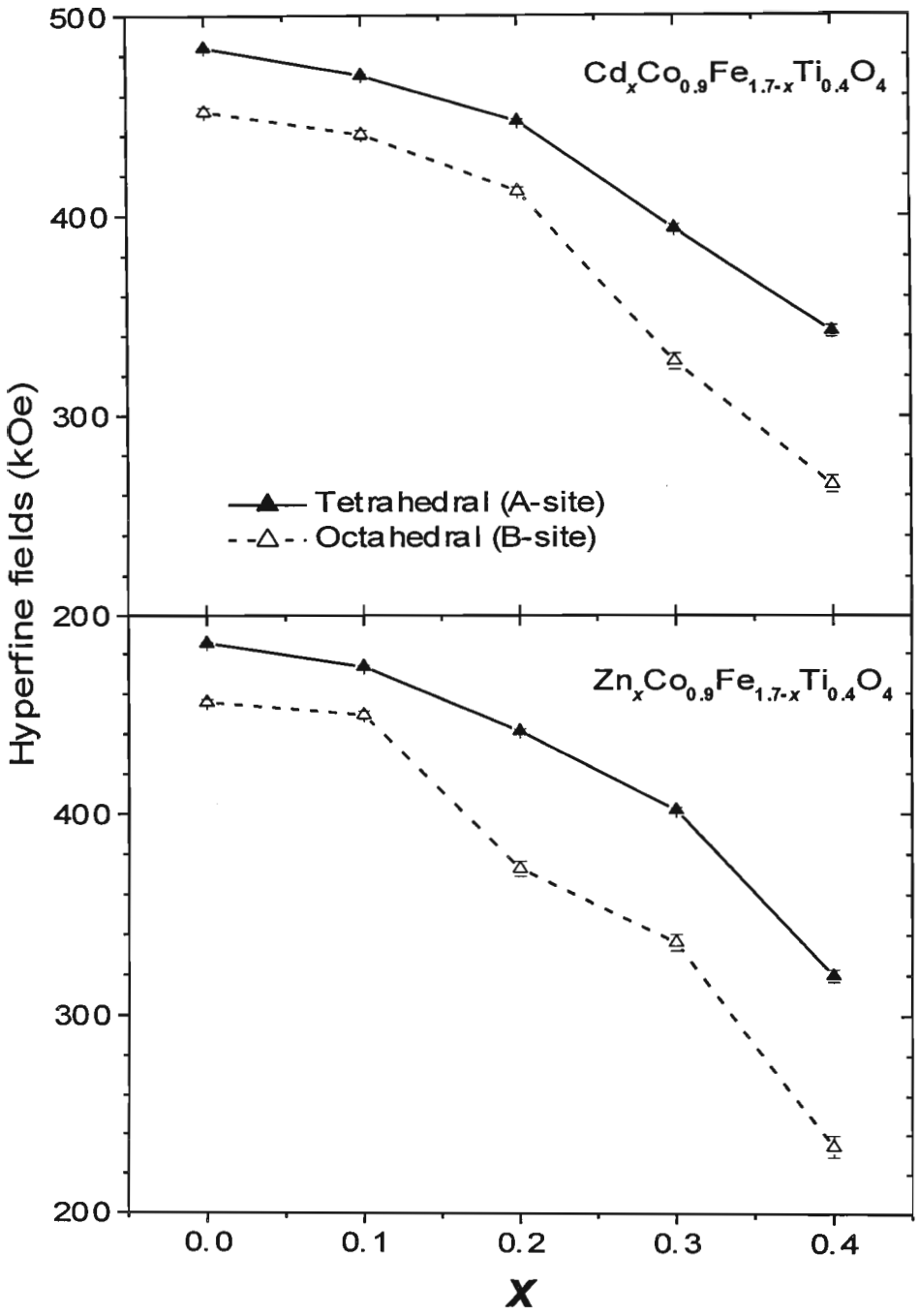

Figure 4.10: Hyperfine fields for (Cd, Zn)$_x$Co$_{0.9}$Fe$_{1.7-x}$Ti$_{0.4}$O$_4$.

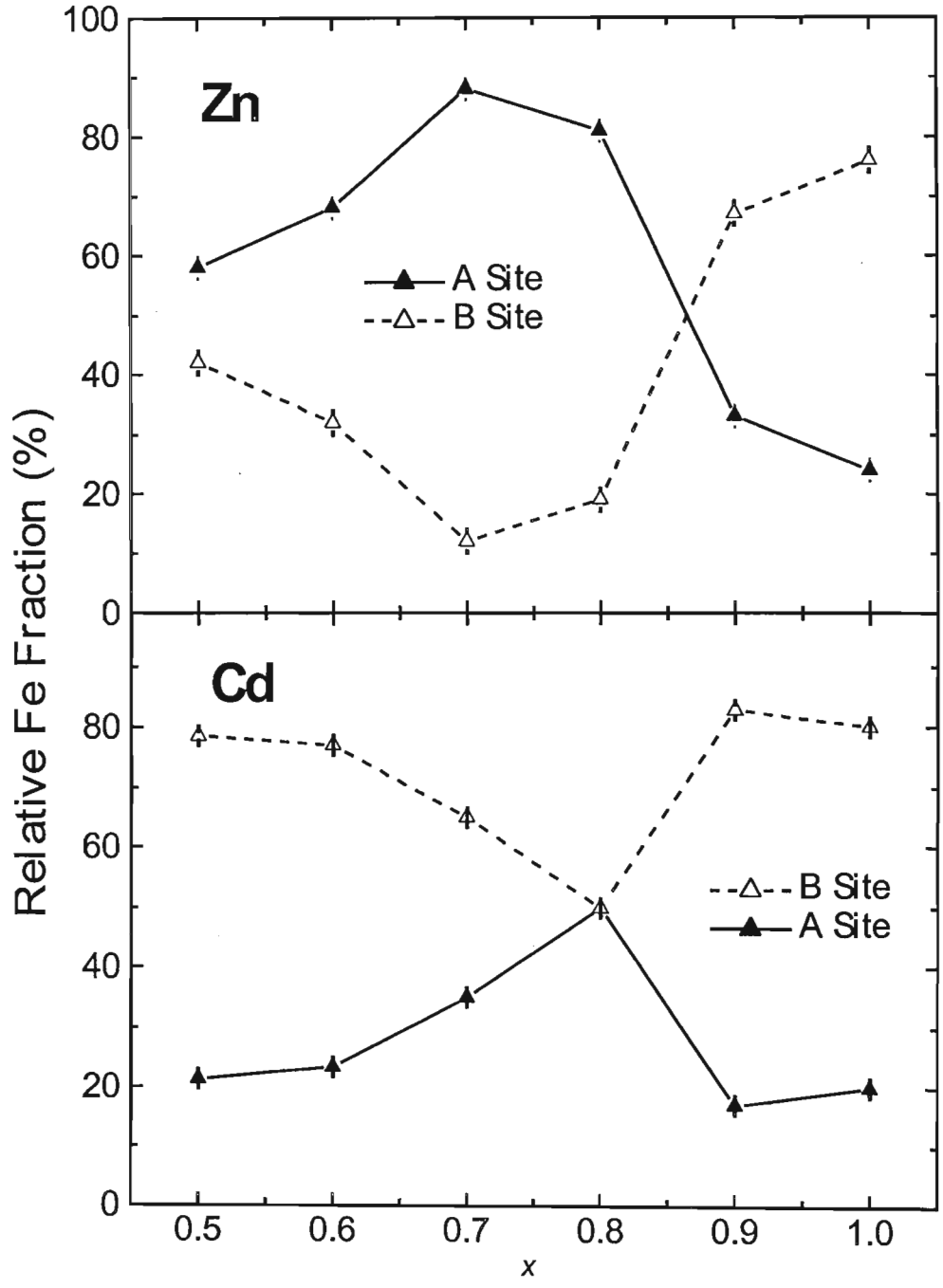

Figure 4.11: Relative proportion of Fe fraction on A and B sites for (Cd, $Zn)_xCo_{0.9}Fe_{1.7-x}Ti_{0.4}O_4$.

the Fe fraction to 0% would be observed. A broad maximum in the Fe fraction was observed around x=0.7 on A site and minimum on B site for Zn based compounds. A maximum in the Fe fraction was observed around x=0.8 on A site and a minimum on B site for Cd based compounds. A systematic decrease of Fe atoms on A site with x to zero at x=1 does not occur. This can be explained if Cd^{2+} and Zn^{2+} ions are also going to B site. These results are in contradiction with the commonly assumed cation distribution [8, 16] given by equation (4.1.1) which assumes that all the diamagnetic Cd or Zn ions go to A site only. The occupation of B sites by Zn ions is one of the models which has been used to explain the reduction of the magnetization above x=0.5 in $Zn_xCo_{1-x}Fe_2O_4$ [6]. Morrish and Haneda [35] have also reported that many preparation conditions of Zn–ferrites can lead to some Zn on B sites.

Chapter 5

The (Cd, Zn)$_x$Co$_{1-x}$Fe$_{2-x}$Al$_x$O$_4$ spinel system

5.1 Introduction

According to the literature cobalt ferrite ($CoFe_2O_4$) is an inverse spinel. When the A site of this compound was diluted by Cd or Zn, migration of Fe ions to B site was observed [6, 5]. This indicates a change to a normal spinel and that Cd or Zn goes to A site. However as discussed in section 1.4, a preliminary study [17] of similar compounds showed that Zn seemed to be going to B site as well. Pettit and Forester [6] suspected this behavior at high concentrations of Zn ions. Al is also known to have preference for the B site in a spinel structure [8]. In this chapter the results and discussions of the effect of simultaneous dilution of both A and B sites by Cd or Zn and Al respectively are presented for the composition range $0 \leq x \leq 1$ in the series (Cd, Zn)$_x$Co$_{1-x}$Fe$_{2-x}$Al$_x$O$_4$.

5.2 X–ray diffraction results

The x–ray diffraction (XRD) patterns for Zn based ($Zn_xCo_{1-x}Fe_{2-x}Al_xO_4$) and for Cd based ($Cd_xCo_{1-x}Fe_{2-x}Al_xO_4$) samples are shown in Figures 5.1 and 5.2 respectively. Sharp x-ray diffraction lines were obtained for all samples except

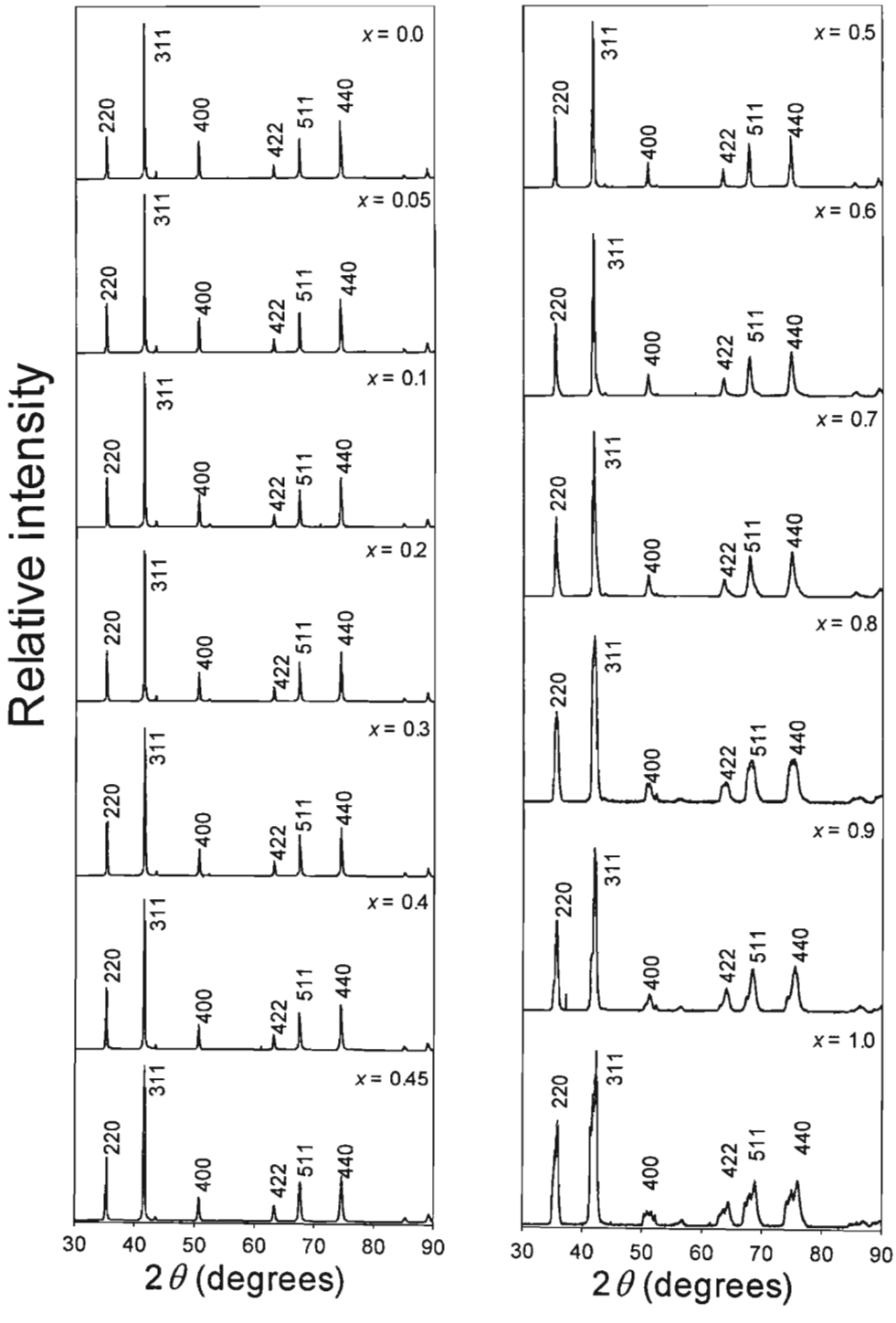

Figure 5.1: X–ray diffraction patterns for $Zn_xCo_{1-x}Fe_{2-x}Al_xO_4$.

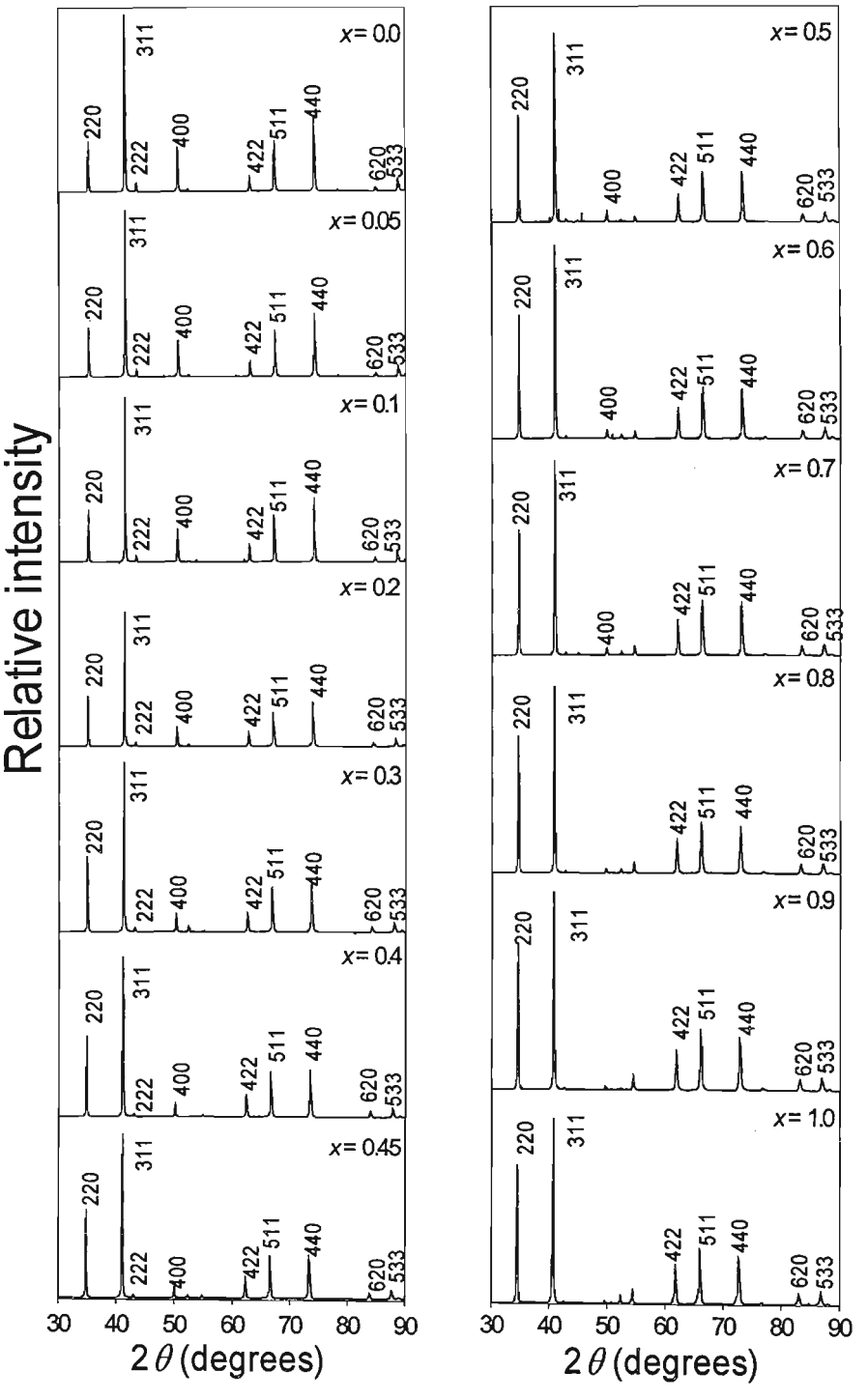

Figure 5.2: X–ray diffraction patterns for $Cd_xCo_{1-x}Fe_{2-x}Al_xO_4$.

for $x \geq 0.80$ in the Zn based samples. The most significant lines were successfully indexed using the XRD data for magnetite [32]. The indexed diffraction lines therefore confirm a single–phase cubic spinel structure in the samples. This means that there is no significant impurity phases in the compounds. Simultaneous dilution of A and B sites appears to have been achieved. The diffraction peaks are fairly broad for $x \geq 0.8$ in Zn based compounds. This might indicate a change from cubic to non–cubic symmetry at very high concentrations of Zn and Al ions or insufficient sintering temperature. Lattice parameters, densities, percentage porosity and grain sizes derived from XRD patterns as discussed in chapter 4 are presented in the following sections.

5.2.1 Lattice parameters

The values of the lattice parameter a found in the samples (see tables 5.1 and 5.2) studied in the present experiment compare very well with previously reported [1, 12, 21, 23] values for similar compounds. The values of a are plotted against x in Figure 5.3. The lattice parameter changes linearly with x, obeying Vergad's law [19]. In Cd based compounds a increases with x. This indicates expansion of the unit cell with Cd and Al substitution. For Zn substituted compounds, a decreases with increase in x indicating contraction of the unit cell with Zn and Al substitution. The variation of a with x is attributed to the size difference and the distribution of cations involved on A and B sites. For the compounds with chemical composition $(\mathrm{Cd, Zn})_x\mathrm{Co}_{1-x}\mathrm{Fe}_{2-x}\mathrm{Al}_x\mathrm{O}_4$, the general cation distribution given by equation (1.4.1) becomes [8]

$$\left(M_x^{2+}\mathrm{Fe}_{1-x}^{3+}\right)^{\mathrm{A}}\left(\mathrm{Co}_{1-x}^{2+}\mathrm{Fe}_{1.0}^{3+}\mathrm{Al}_x^{3+}\right)^{\mathrm{B}}\mathrm{O}_4^{2-} \tag{5.2.1}$$

where M is Cd or Zn. This cation distribution assumes that all the Zn^{2+} or Cd^{2+} and the Al^{3+} ions are replacing Fe^{3+} and Co^{2+} on A and B sites respectively. The tetrahedral radius R_{A} and octahedral radius R_{B} for Cd or Zn based samples can be calculated from the cation distribution given by equation (5.2.1). From this cation distribution the tetrahedral and octahedral

Table 5.1: Bulk ρ_b and X-ray ρ_x densities, porosity P and lattice parameter a for $Zn_xCo_{1-x}Fe_{2-x}Al_xO_4$.

x	ρ_b (g/cm^3)	ρ_x (g/cm^3)	P (%)	a ($\AA$)
	$\pm$ 0.03	$\pm$ 0.01	$\pm$ 0.1	$\pm$ 0.01
0	3.66	5.30	30.9	8.38
0.05	3.80	5.28	28.0	8.38
0.1	3.89	5.26	26.1	8.37
0.2	3.89	5.22	25.5	8.37
0.3	3.76	5.19	27.6	8.35
0.4	3.63	5.14	29.3	8.35
0.45	3.19	5.15	38.0	8.34
0.5	3.37	5.13	34.2	8.33
0.6	3.27	5.11	35.9	8.32
0.7	3.02	5.08	40.5	8.30
0.8	3.17	5.05	37.1	8.29
0.85	3.00	5.06	40.9	8.27
0.9	3.00	5.06	40.7	8.27
0.95	2.92	5.04	42.1	8.25
1.0	2.91	5.42	41.9	8.26

Table 5.2: Bulk ρ_b and X-ray ρ_x densities, porosity P and lattice parameter a for $Cd_xCo_{1-x}Fe_{2-x}Al_xO_4$.

x	ρ_b (g/cm^3)	ρ_x (g/cm^3)	P (%)	a ($\AA$)
	$\pm$ 0.03	$\pm$ 0.01	$\pm$ 0.1	$\pm$ 0.01
0	4.01	5.30	24.3	8.38
0.05	3.93	5.32	26.2	8.38
0.1	3.96	5.32	25.6	8.40
0.2	4.19	5.34	21.5	8.42
0.3	4.30	5.36	19.7	8.43
0.4	4.72	5.38	12.2	8.45
0.45	4.68	5.39	13.2	8.46
0.5	4.59	5.39	14.9	8.47
0.6	4.92	5.42	9.3	8.49
0.7	5.00	5.45	8.2	8.50
0.8	4.97	5.48	9.4	8.51
0.9	4.73	5.51	14.3	8.52
1.0	4.89	5.55	11.9	8.53

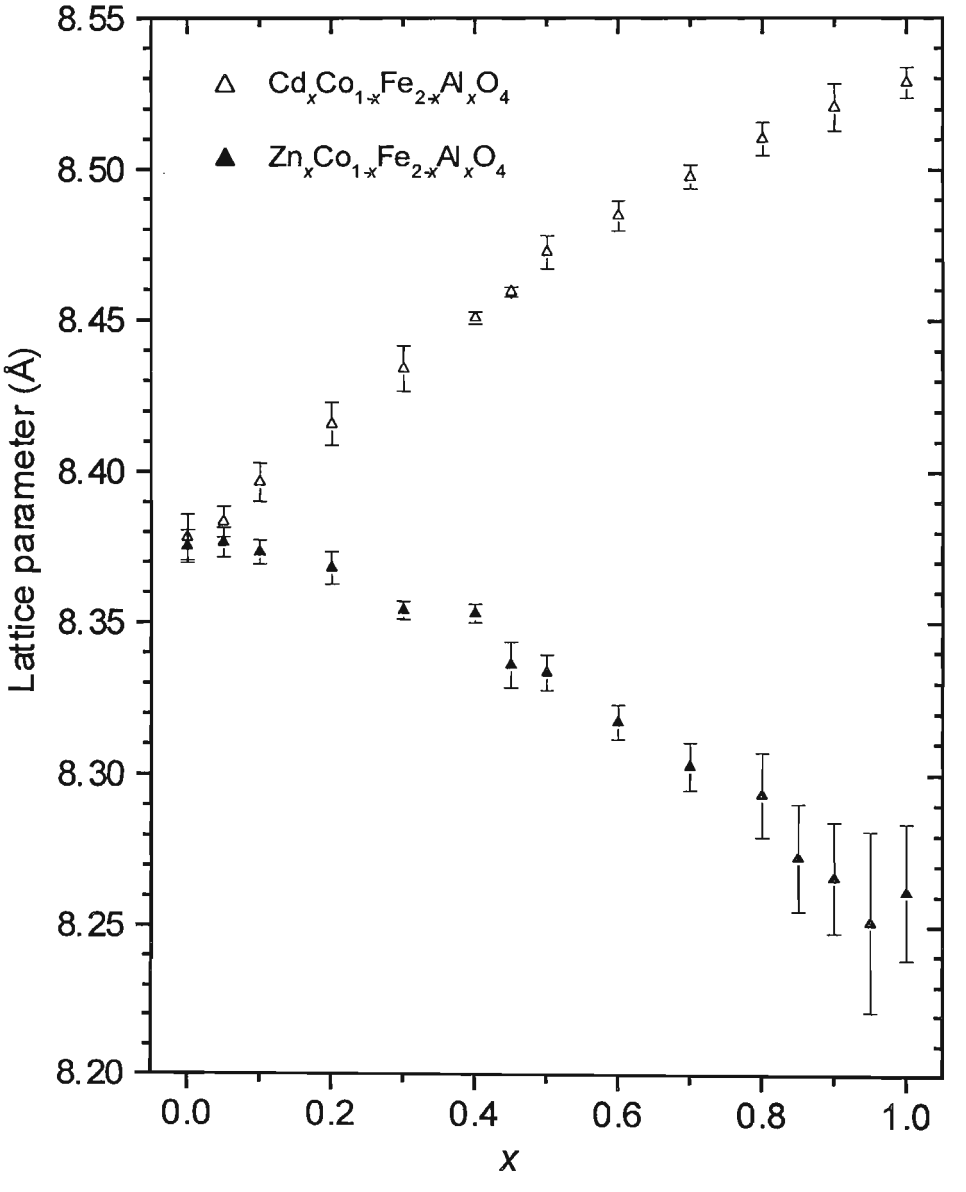

Figure 5.3: Lattice parameters of (Cd, Zn)$_x$Co$_{1-x}$Fe$_{2-x}$Al$_x$O$_4$.

radii are

$$R_{\mathrm{A}} = (R_{M^{2+}} - R_{\mathrm{Fe}^{3+}})x + R_{\mathrm{Fe}^{3+}} \tag{5.2.2}$$

and

$$R_{\mathrm{B}} = \left[(R_{\mathrm{Al}^{3+}} - R_{\mathrm{Co}^{2+}})x + R_{\mathrm{Co}^{2+}} + R_{\mathrm{Fe}^{3+}}\right]/2 \tag{5.2.3}$$

respectively. Using the ionic radii values in table 4.3, the tetrahedral radii are

$$R_{\mathrm{A}}(\mathrm{Cd}) = (0.033x + 0.064)\ \mathrm{nm} \tag{5.2.4}$$

and

$$R_{\mathrm{A}}(\mathrm{Zn}) = (0.010x + 0.064)\ \mathrm{nm}. \tag{5.2.5}$$

In both Cd and Zn based samples

$$R_{\mathrm{B}} = (-0.011x + 0.068)\ \mathrm{nm}. \tag{5.2.6}$$

The variation of R_{A} and R_{B} with x is shown in Figure 5.4. The increase in R_{A} for both Cd and Zn based samples is predicted by the positive slopes in equations (5.2.4) and (5.2.5). Similarly a decrease in R_{B} is predicted from the negative slope in equation (5.2.6). The increase in R_{A} with x in Cd based samples is because on an A site the larger Cd^{2+} ions substitute the smaller Fe^{3+} ions (see table 4.3). Similarly, an increase in R_{A} with x in Zn based samples is because of larger Zn^{2+} ions replacing the smaller Fe^{3+} ions on an A site. The higher increase R_{A} in Cd than in Zn based samples is consistent with larger size of the Cd atom. The decrease in R_{B} with x is because the smaller Al^{3+} substitute the larger Co^{2+} ions on B site. In Cd based compounds the increase in R_{A} is very large compared to the decrease in R_{B}. This results in an expansion of the unit cell and shows as an increase in the lattice parameter with x. An increase in lattice parameters have been observed [9, 18, 21, 23] when larger atoms are replacing smaller atoms in mixed ferrites. In Zn based compounds the increase in R_{A} is lower than the reduction of R_{B} with x. This results in the contraction of the unit cell and shows as reduction in the lattice parameter with x. A decrease in lattice parameters when smaller atoms are substituting bigger atoms has also been reported [19, 20, 22].

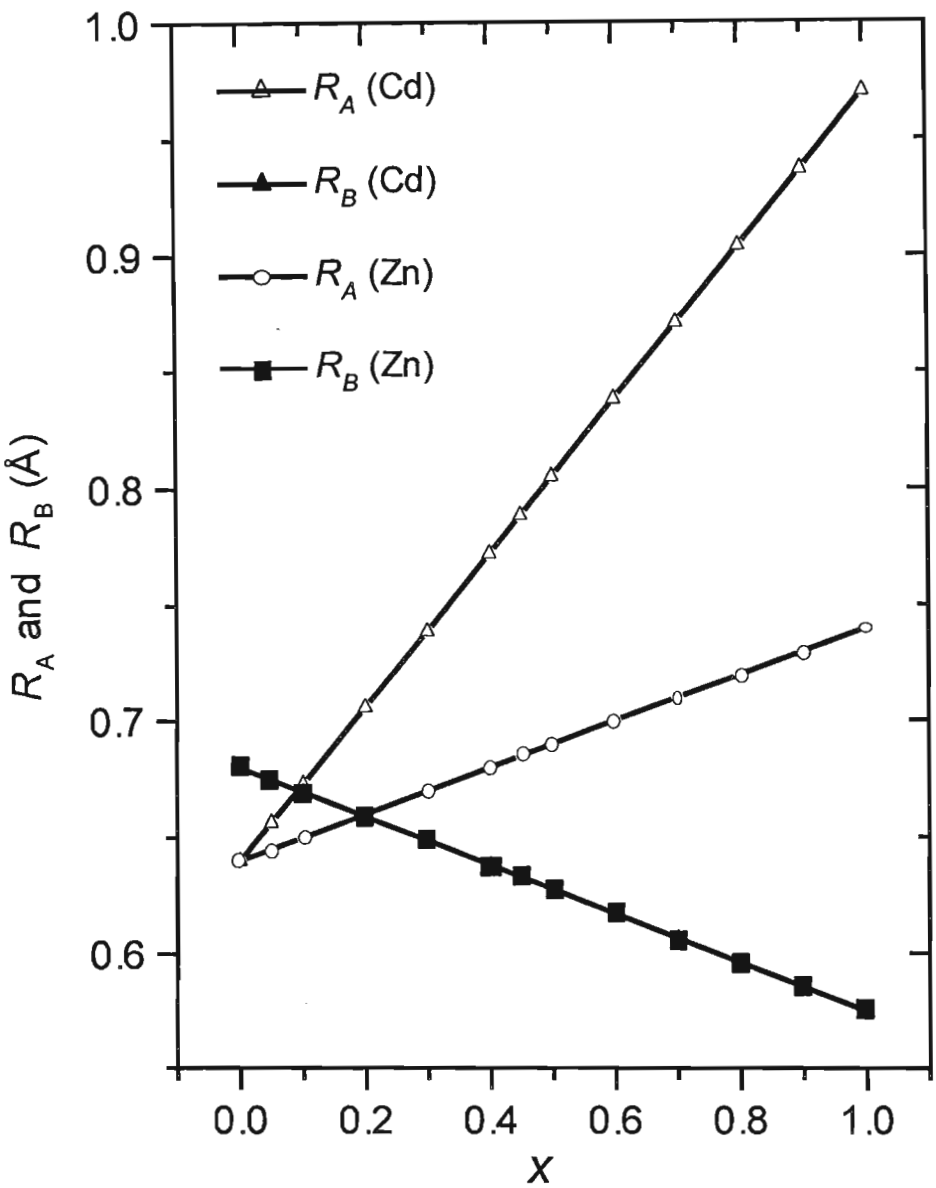

Figure 5.4: Bond lengths as a function of x for (Cd, Zn)$_x$Co$_{1-x}$Fe$_{2-x}$Al$_x$O$_4$.

5.2.2 Bulk and X–ray densities of compounds

The values of X–ray density ρ_x and bulk density ρ_b are shown in tables 5.1 and 5.2 and are plotted in Figure 5.5. These values compare well with those previously reported [1, 23] for similar mixed ferrites. The X-ray densities are higher than the bulk densities. This is due to the existence of empty spaces (voids) in the bulk (samples) which depend on the sintering process. The bulk densities for $Cd_xCo_{1-x}Fe_{2-x}Al_xO_4$ compounds varied between 4.0 g/cm^3 and 5.0 g/cm^3. The increase in density with x is attributed to size difference of ions involved. For $Zn_xCo_{1-x}Fe_{2-x}Al_xO_4$, the bulk densities lie between 2.9 g/cm^3 and 3.9 g/cm^3. In the Cd based compounds X–ray densities increase with x, like the bulk densities. For the Zn based compounds X-ray densities decreased with x, like bulk densities for $x \geq 0.2$. For $x \leq 0.1$ a bulk density minimum in Cd based samples and a bulk density maximum in Zn based samples, was observed.

5.2.3 Porosity of samples

The porosity of the samples were derived from X–ray and bulk densities using equation (4.2.3). The samples produced are highly porous. This is expected to significantly depend on the sample preparation process and heat treatment. There is a general increase and a general decrease with x in porosity for $x \geq 0.1$ in Zn based and Cd based compounds, respectively (see figure 5.6).

5.2.4 Grain sizes in the compounds

Figure 5.7 shows the variation with x of the grain sizes of the compounds. These were calculated from the broadening of the (311) X–ray diffraction line as discussed in chapter 4. The grain sizes of Cd based samples lie between 50 nm and 70 nm. Fluctuations may be related to inconsistences in grinding of samples by hand using mortar and pestle. An anomalous decrease of the grain sizes with x in Zn based compounds for $x \geq 0.4$ was observed. A clear

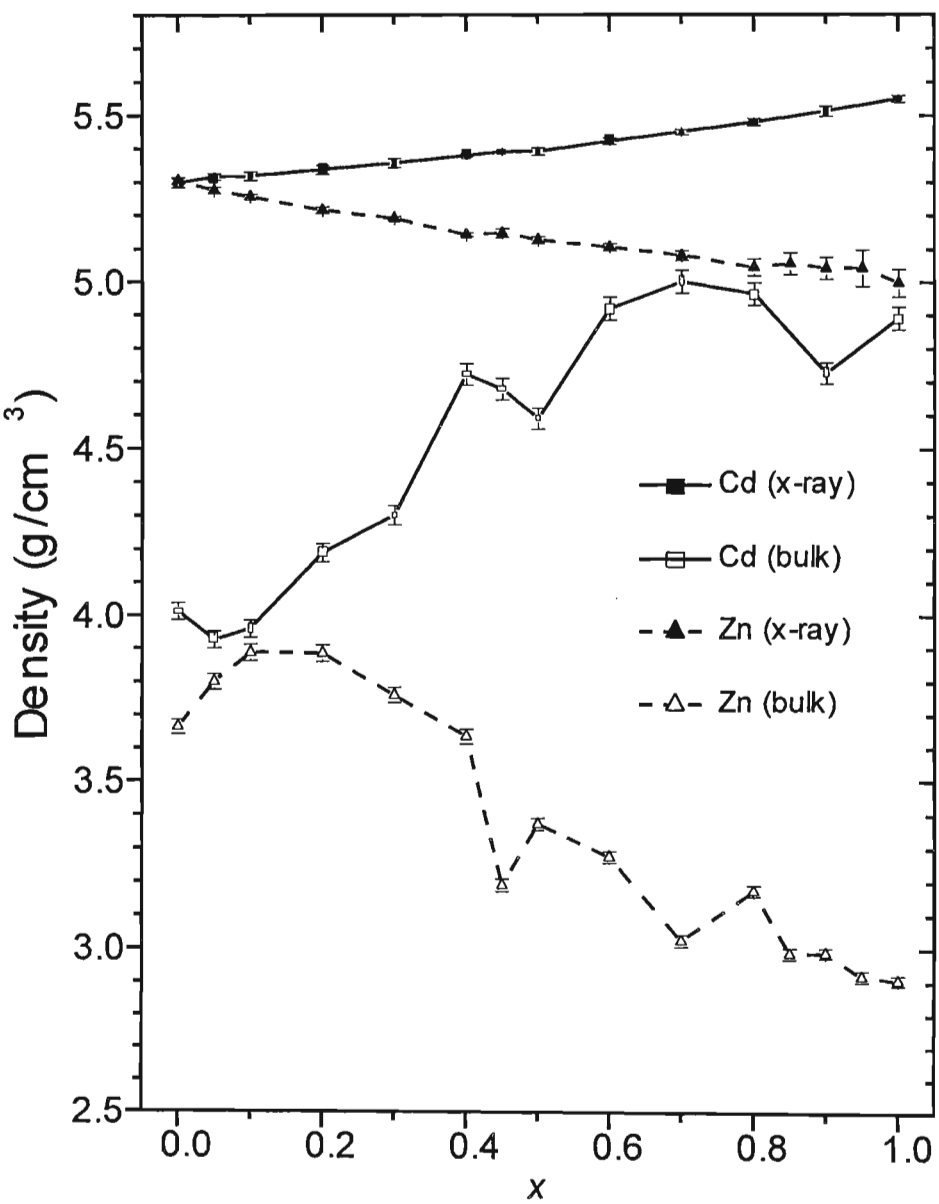

Figure 5.5: Bulk and X–ray densities for (Cd, Zn)$_x$Co$_{1-x}$Fe$_{2-x}$Al$_x$O$_4$.

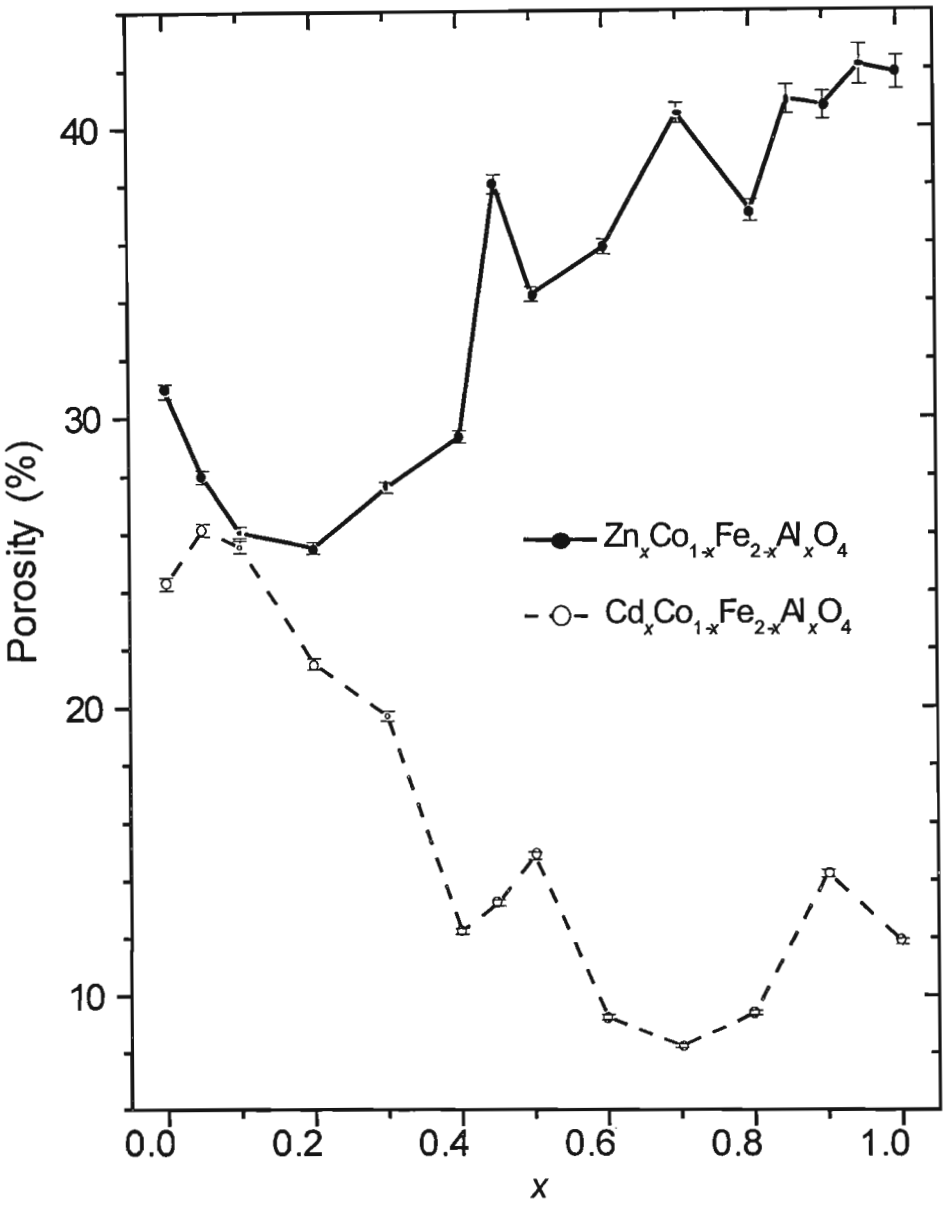

Figure 5.6: Porosity as a function of x for (Cd, Zn)$_x$Co$_{1-x}$Fe$_{2-x}$Al$_x$O$_4$.

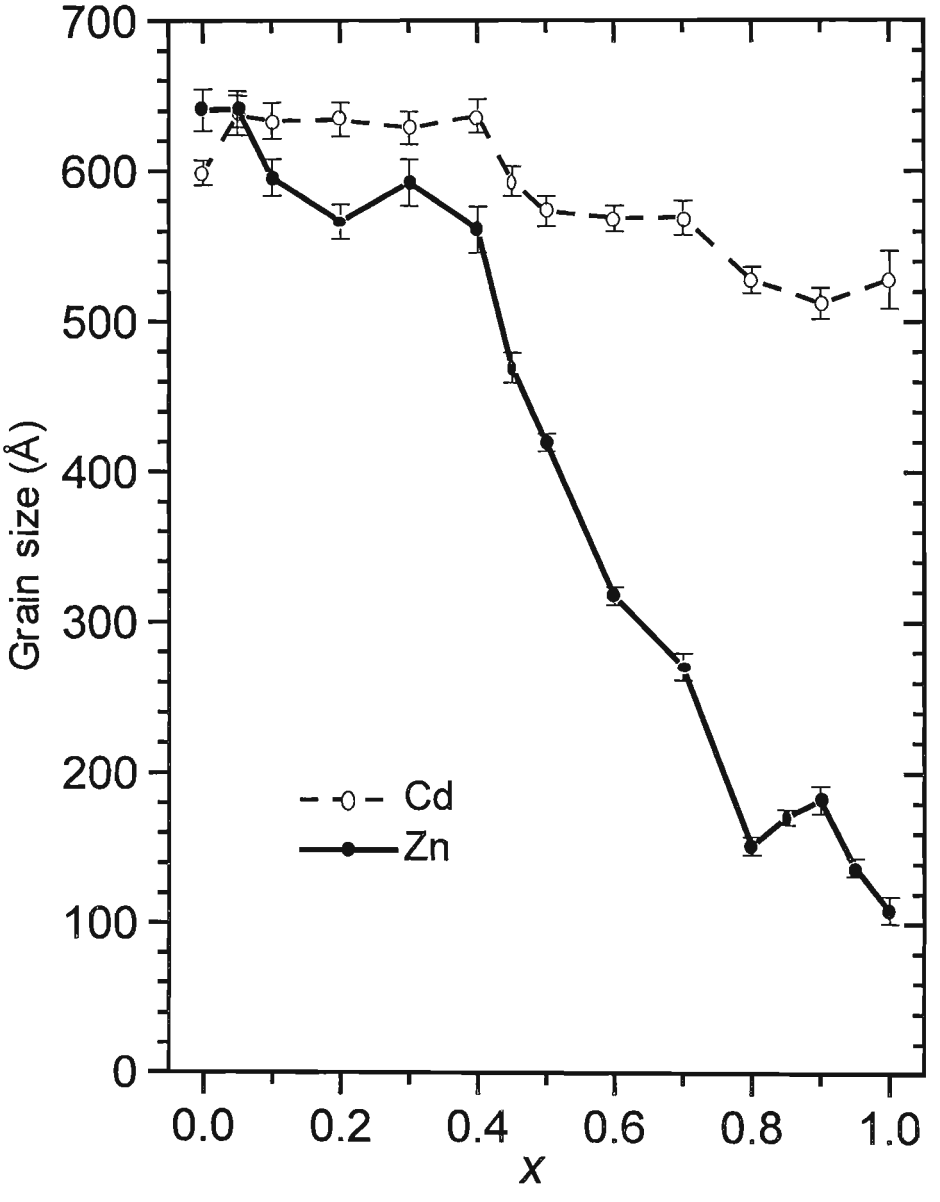

Figure 5.7: Grain sizes for (Cd, Zn)$_x$Co$_{1-x}$Fe$_{2-x}$Al$_x$O$_4$.

explanation for this effect is not available.

5.3 Mössbauer spectroscopy results

The compositional dependences of the Mössbauer spectra for $Zn_xCo_{1-x}Fe_{2-x}Al_xO_4$ and $Cd_xCo_{1-x}Fe_{2-x}Al_xO_4$ compounds are shown in Figures 5.8 and 5.9 respectively. The closely related behaviour of the samples is attributed to the similar electronic configurations of the Cd and Zn atoms. The well resolved magnetic split sextets are observed for $x \leq 0.3$. The six line Mössbauer spectra revealed the ferrimagnetic behavior of the samples. As the concentration of diamagnetic ions is increased, both Cd and Zn based compounds transform at about $x=0.45$ from an ordered magnetic state to a paramagnetic state, which is revealed by a change from magnetic split sextets to paramagnetic doublets in the spectra. The region $0.4<x\leq 0.6$ has been reported by Thanki et al [8] as the relaxed region and they made no attempt to analyze the Mössbauer spectra in this region. The spectra in the relaxed region consisted of paramagnetic components in addition to magnetic split sextets. The change of the magnetic phase is due to dilution of magnetic Fe and Co ions by diamagnetic ions. This results in broken exchange paths via the oxygen ions between the Fe ions on A and those on B sites. As a result, the superexchange interactions between the A and the B sublattice weakens. This gives rise to a paramagnetic state revealed by paramagnetic doublets in the Mössbauer spectra.

The solid lines through data points in Figures 5.8 and 5.9 are the result of the computer fits obtained using the Recoil Mössbauer spectral analysis software [30]. Zero quadrupole splitting for $x \leq 0.45$ was again assumed. Negligible quadrupole splitting was observed by Thanki et al [8] in Zn based compounds. For $x \leq 0.3$ the spectra were fitted with two sextets. For $0.4<x<0.5$ the spectra were fitted with doublets and sextets. In the range $0.6<x<1.0$, spectra were fitted with two symmetric doublets. Sextets or doublets with lower values of quadrupole splitting and isomer shifts were assigned to A sites. The reason for

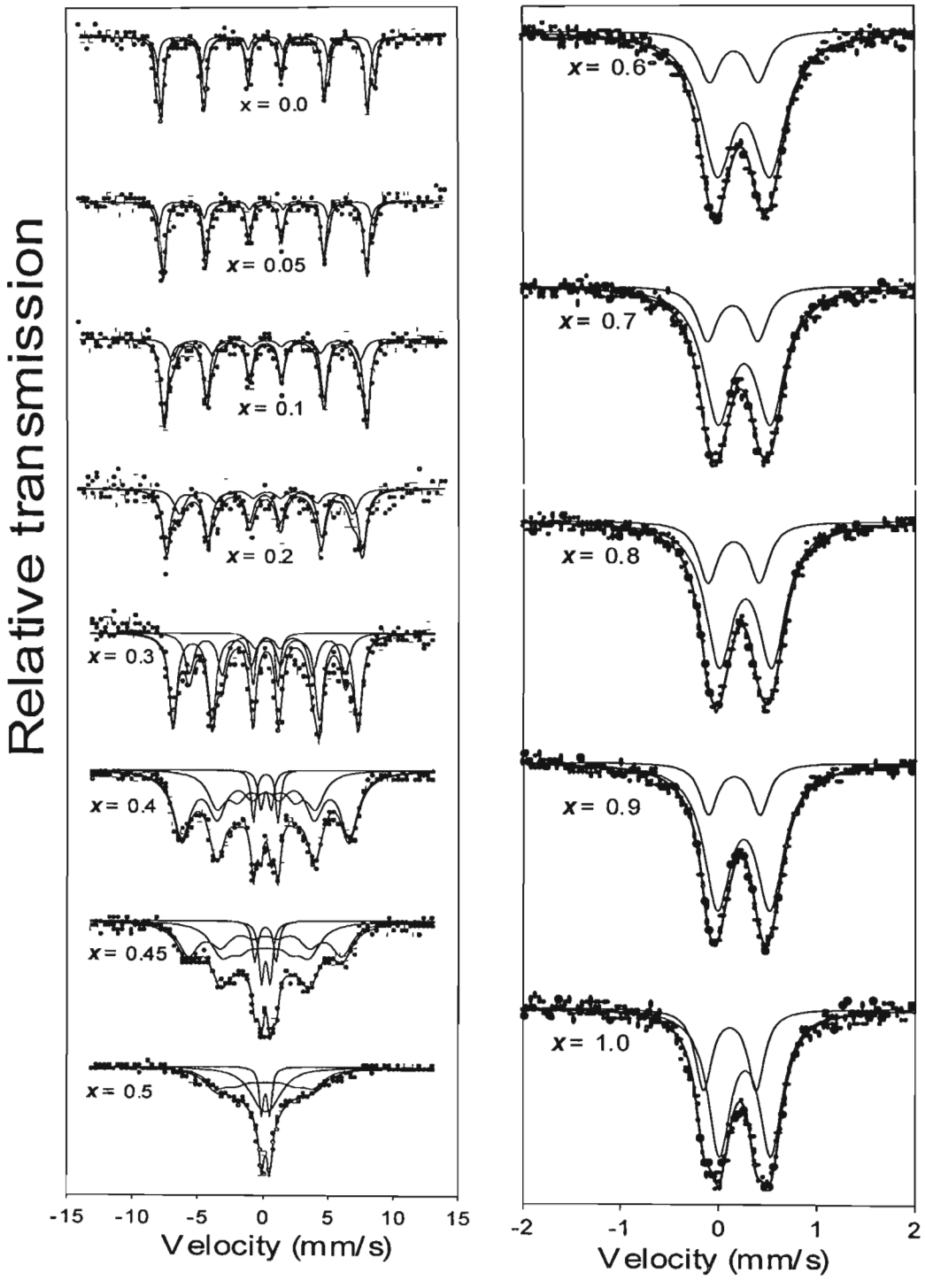

Figure 5.8: Mössbauer spectra for $Zn_xCo_{1-x}Fe_{2-x}Al_xO_4$.

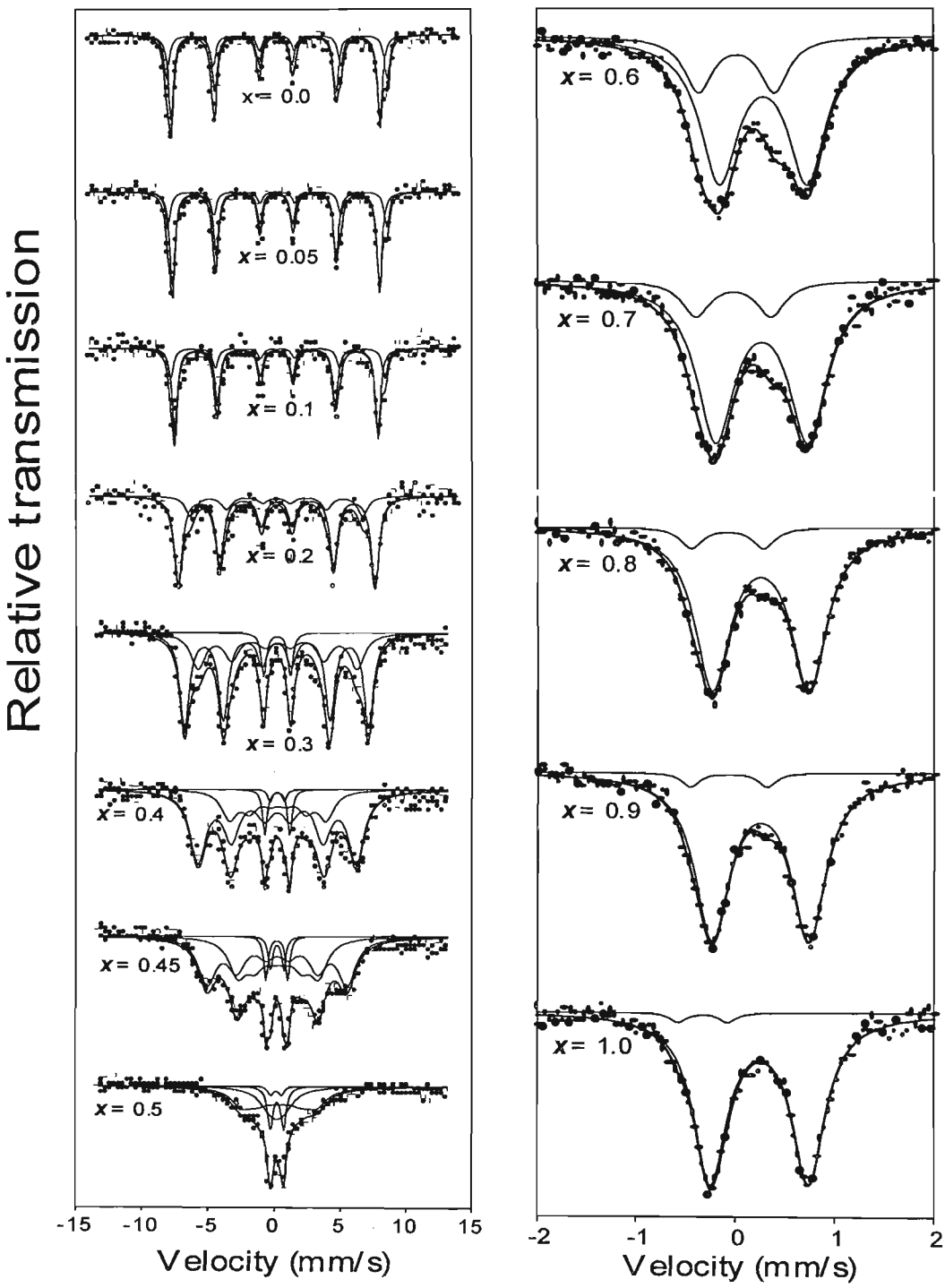

Figure 5.9: Mössbauer spectra for $Cd_xCo_{1-x}Fe_{2-x}Al_xO_4$.

this was given in section (4.1.6).

The values of isomer shifts, quadrupole splitting and hyperfine fields for Cd and Zn based samples are shown in tables 5.3 and 5.4. The average isomer shift and quadrupole splitting values are shown in table 5.5. The isomer shifts values of 0.16 mm/s and 0.27 mm/s on A and B sites respectively were found for a cobalt ferrite (x=0 in table 5.3). Similar values were reported by Seung et al [34] and correspond to the high spin Fe^{3+} charge state. The present values therefore indicate that Fe ions exist in high spin Fe^{3+} state only. There is no significant variation of isomer shift with x observed in Zn based samples, meaning that the s-electron charge distribution of Fe^{3+} is not significantly affected by Zn or Cd content, either on an A or a B site. In Cd based compounds the isomer shift decreases with an increase in x on an A site for $x \geq 0.5$. A similar behavior was found by Amer and Hemeda [5] when the A site of the cobalt ferrite was diluted by Cd. This means that the s-electron charge distribution of Fe^{3+} on an A site is affected by a high concentration of Cd ions. This suggests that Cd has more preference for A site compared to Zn at higher concentrations. This effect has also been revealed by XRD data. The isomer shifts on B sites are larger than those on A sites as expected. The values for quadrupole splitting on a B site are also larger than on an A site. This behavior is expected since there exists low symmetry on the octahedral site resulting in high electric field gradients in the B site of the ^{57}Fe nucleus. There is no significant variation in the quadrupole splitting with x observed. However, Cd based compounds have generally higher quadrupole splitting and isomer shift compared to Zn based compounds. Higher quadrupole splitting and isomer shift in $CdFe_2O_4$ than in $ZnFe_2O_4$ ferrites was reported by Gibbs [2]. This means that Zn compounds have higher degree of covalency compared to Cd compounds. This compares well with the shorter bond length of Zn based compared to Cd based samples (see figure 5.4) predicted by the general cation distribution [1, 8]. Shorter bond length indicates high covalency in a compound.

In Figure 5.10 the composition dependence of hyperfine fields on an A and

Table 5.3: Isomer shift (IS), quadrupole splitting (QS) and hyperfine fields (H) for $Zn_xCo_{1-x}Fe_{2-x}Al_xO_4$.

	IS (mm/s)		QS (mm/s)		H (kOe)	
x	$(IS)_A$	$(IS)_B$	$(QS)_A$	$(QS)_B$	$(H)_A$	$(H)_B$
	± 0.03	± 0.03	± 0.002	±0.006	±8	±2
0	0.16	0.27			519	490
0.05	0.17	0.27			510	483
0.1	0.18	0.24			446	482
0.2	0.10	0.23			412	466
0.3	0.18	0.31			370	440
0.4	0.19	0.22			234	398
0.45	0.17	0.18			210	364
0.5	0.18	0.23	0.499	0.532		
0.6	0.17	0.26	0.516	0.535		
0.7	0.14	0.26	0.523	0.536		
0.8	0.15	0.27	0.526	0.537		
0.9	0.16	0.25	0.548	0.524		
1.0	0.12	0.27	0.537	0.001		

Table 5.4: Isomer shift (IS), quadrupole splitting (QS) and hyperfine fields (H) for $Cd_xCo_{1-x}Fe_{2-x}Al_xO_4$.

	IS (mm/s)		QS (mm/s)		H (kOe)	
x	$(IS)_A$	$(IS)_B$	$(QS)_A$	$(QS)_B$	$(H)_A$	$(H)_B$
	± 0.03	± 0.03	± 0.02	±0.06	±8	±2
0	0.16	0.26			519	491
0.05	0.17	0.26			515	486
0.1	0.16	0.27			503	478
0.2	0.18	0.16			405	462
0.3	0.18	0.25			373	432
0.4	0.22	0.26			227	371
0.45	0.22	0.31			190	328
0.5	0.39	0.21			35	176
0.6	0.09	0.21	0.76	0.89		
0.7	-0.02	0.27	0.76	0.89		
0.8	-0.08	0.26	0.73	0.97		
0.9	-0.07	0.25	0.77	0.98		
1.0	-0.33	0.25	0.50	0.99		

Table 5.5: Average values of isomer shifts (IS) and quadrupole splitting (QS) of sextets or doublets for (Cd, Zn)$_x$Co$_{1-x}$Fe$_{2-x}$Al$_x$O$_4$.

	Zn–based spinel		Cd–based spinel	
Parameter	(mm/s)	x	(mm/s)	x
$< \text{IS} >_\text{A}$	0.15±0.03	(0.0<x<1.0)	0.18±0.03	(0.0<x<1.0)
$< \text{IS} >_\text{B}$	0.25±0.03	(0.0<x<1.0)	0.25±0.04	(0.0<x<1.0)
$< \text{QS} >_\text{A}$	0.52±0.02	($x \geq$ 0.6)	0.75±0.02	($x \geq$0.6)
$< \text{QS} >_\text{B}$	0.534±0.006	($x \geq$0.6)	0.94±0.04	($x \geq$0.6)

a B sites is shown. A systematic decrease of hyperfine fields with x indicates the weakening of the magnetic coupling. This is expected because magnetic coupling depends on magnetic neighbors present in the Fe environment. The decrease on a B site with an increase in x happens because the diamagnetic Al^{3+} ions replace the magnetic Co^{2+}. Similarly, a decrease in hyperfine fields on an A site is due to replacement of Fe^{3+} ions by the diamagnetic Cd^{2+} ions. A cross over effect with respect to hyperfine fields on A and B sites is observed, which happens at low levels of Cd or Zn dilution.

The area of a sextet or doublet in a Mössbauer spectra reflects the relative fraction of Fe atoms on A or B site, and hence, inversely, the occupation of these sites by the Cd or Zn and Al ions. This is plotted with x in Figure 5.11. The trends are similar for both series of compounds. A maximum in the Fe fraction on an A site at low values of x is observed. This can be attributed to the occupation of both A and B sites by Cd and Zn atoms. In Cd based spinels for x>0.4, there is a gradual decrease of Fe atoms on A sites and an increase on B sites. This is the expected trend if Cd and Al ions have preference for A and B sites respectively. In Zn based spinels, the situation appears to be more complicated and contradicts the cation distribution assumed earlier [8]. A broad peak in the Fe fraction on the A site reappears in the range 0.6$\leq x \leq$0.95

suggesting again that Zn atoms go to both sites. A systematic reduction in the proportion of Fe atoms on A site to zero does not occur for Zn based samples.

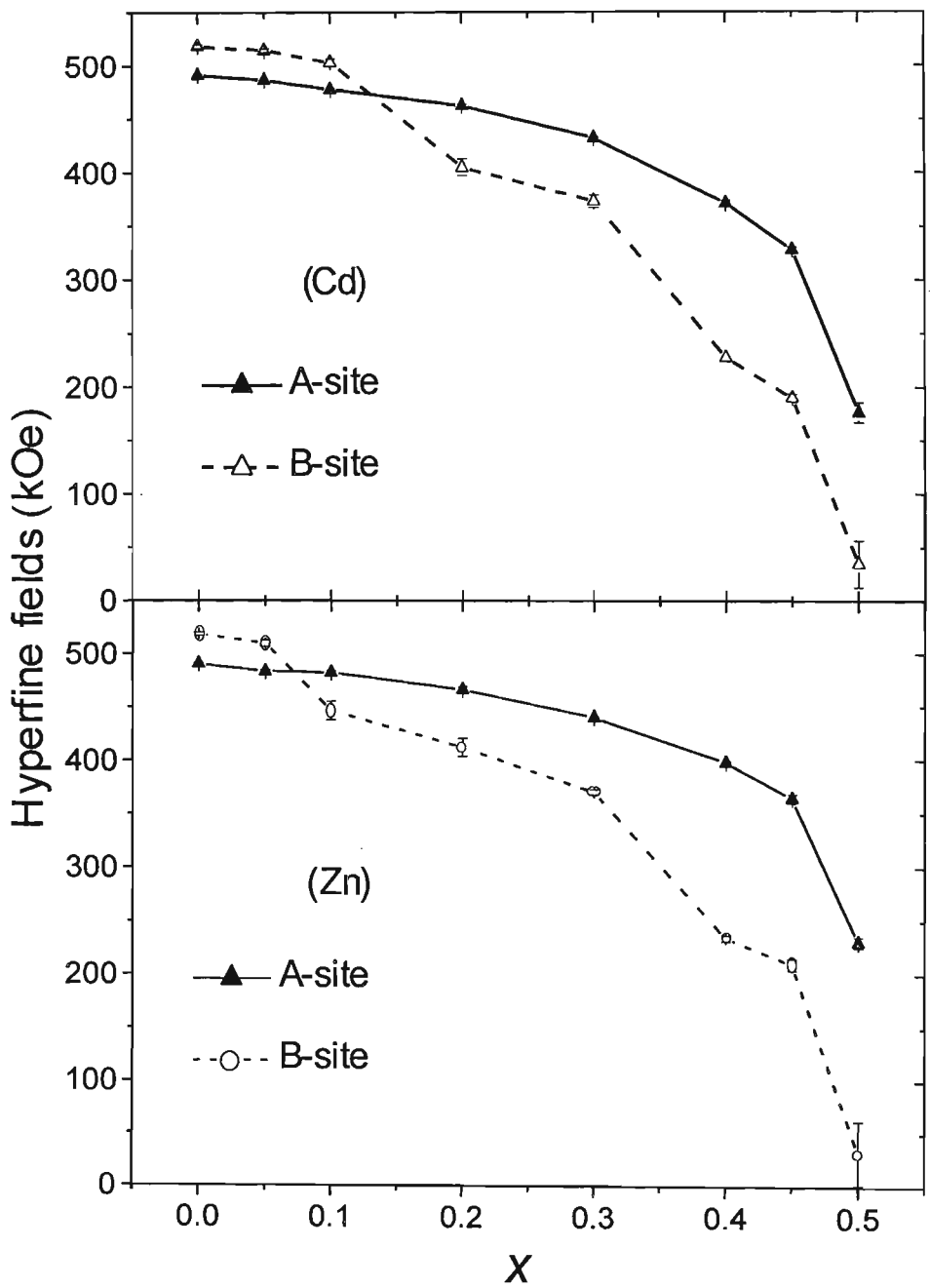

Figure 5.10: Hyperfine fields for (Cd, Zn)$_x$Co$_{1-x}$Fe$_{2-x}$Al$_x$O$_4$.

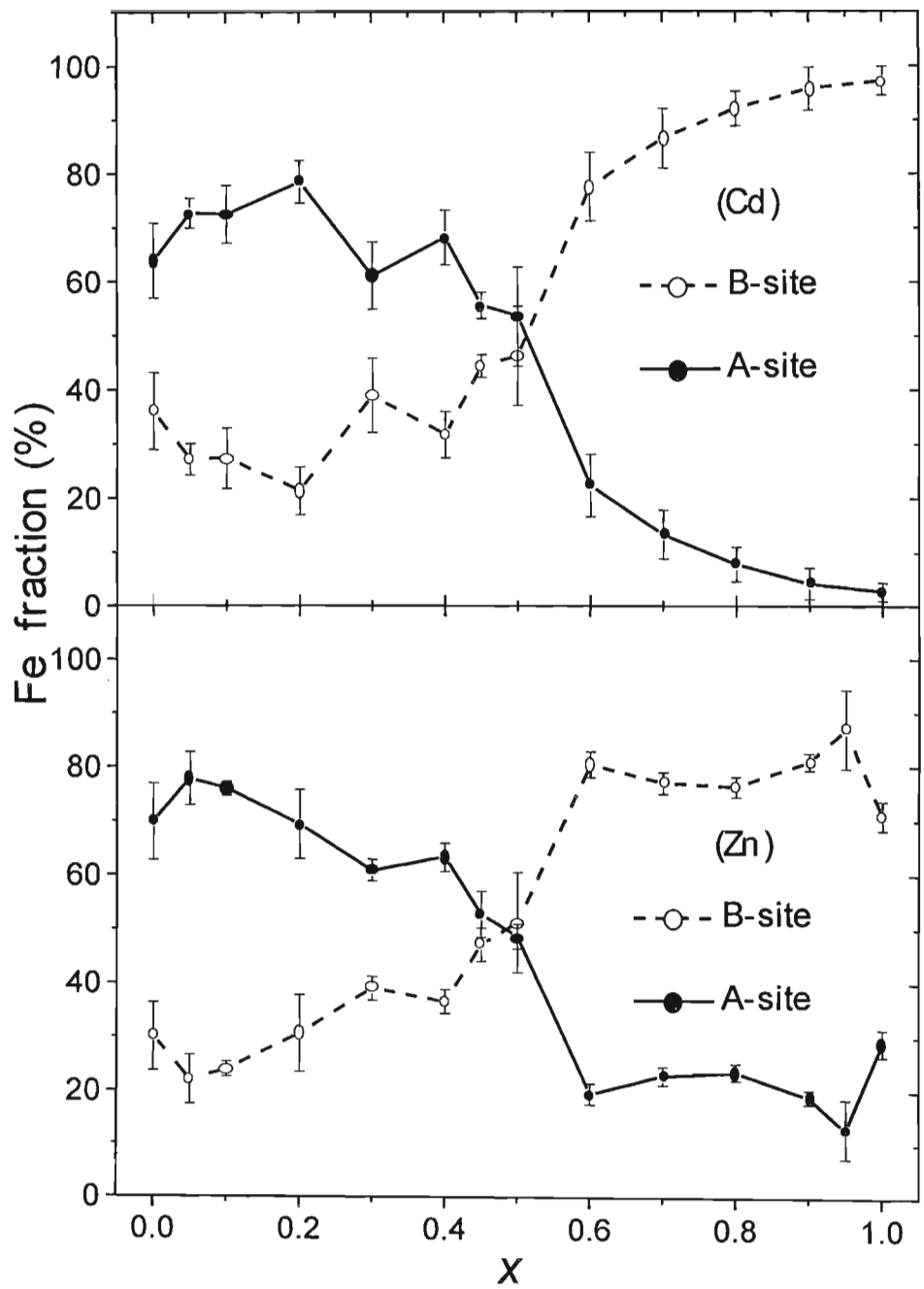

Figure 5.11: Relative proportion of Fe fraction on A and B sites for (Cd, Zn)$_x$Co$_{1-x}$Fe$_{2-x}$Al$_x$O$_4$.

Chapter 6

Conclusions

Mössbauer spectroscopy and powder x–ray diffraction measurements of (Cd, $Zn)_xCo_{0.9}Fe_{1.7-x}Ti_{0.4}O_4$ and (Cd, $Zn)_xCo_{1-x}Fe_{2-x}Al_xO_4$ compounds in the range $0 \leq x \leq 1.0$, have been carried out. Samples were prepared by a standard ceramic process and showed no significant impurity phases. All samples crystallized with a single phase cubic spinel, which indicates that both double and single site dilution appear to have been achieved.

The values of lattice parameters, bulk and x–ray densities compare well with those found for similar mixed ferrites. The variation of the lattice constant with x is attributed to the size difference of the cations involved. This agrees well with the variation of tetrahedral and octahedral radii predicted by the general distribution of cations [1, 8, 16] on A and B sites. However, at high concentrations of x there was a deviation from the expected behavior of the lattice constants. The deviation was more rapid for Zn based compounds and can be explained if Cd or Zn goes to a B site as well when in high concentrations. A more gradual change of the lattice constant with Cd substitution was observed. This reveals the effect of the larger size of the Cd atom.

For the (Cd, $Zn)_xCo_{1-x}Fe_{2-x}Al_xO_4$ compounds, both bulk and X–ray densities were found to increase in Cd and a decrease with Zn dilution. Although a general increase in both x–ray and bulk densities are observed with x for (Cd, $Zn)_xCo_{0.9}Fe_{1.7-x}Ti_{0.4}O_4$ compounds, the bulk density fluctuates with Zn sub-

stitution. The samples produced in this work are highly porous. An anomalous decrease of grain sizes with x was obtained for $Zn_xCo_{1-x}Fe_{2-x}Al_xO_4$ samples. The densities, porosity and grain sizes of samples depend on the sample preparation method and conditions. It would be advisable to produce the samples in a future project using high energy ball milling in order to see if the reduction in grain sizes with x is a genuine effect for Zn and Al substituted compounds.

The Mössbauer spectra show that the relaxation effects take place at high values of x when the cobalt ferrite is simultaneously diluted on both an A and a B site than when it was diluted on a single site by Cd or Zn [5, 6]. This shows that the frustration effects and spin disordering takes place faster when dilution takes place simultaneously on both A and B sites. A similar behavior has been found in Zn based compounds [8].

The isomer shift reflects that Fe atoms exist in high spin Fe^{3+} state in the present series of compounds. Similar results were obtained by Thanki et al [8] in Zn based samples. Both isomer shifts and quadrupole splitting have been found to be generally higher in Cd based than in Zn based compounds. This indicates a higher degree of covalency in iron oxygen bond in Zn based compounds. The same effect was observed by Gibbs [2]. The decrease in hyperfine fields with x is attributed to the weakening of the magnetic coupling as the magnetic ions are being diluted with diamagnetic ions. A cross over effect with respect to hyperfine fields is observed in $(Cd, Zn)_xCo_{1-x}Fe_{2-x}Al_xO_4$ but not in $(Cd, Zn)_xCo_{0.9}Fe_{1.7-x}Ti_{0.4}O_4$ compounds. This effect still needs further investigation.

The magnetic properties investigated in this work are similar to those found by Thanki et al [8] in Zn based compounds. There was no indication of the effect of preparing the samples in flowing oxygen than in air. The magnetic properties of Cd and Zn based samples investigated, appear to be similar, as expected. However, the present results show that the diamagnetic Cd^{2+} and Zn^{2+} ions are replacing Fe ions on both A and B sites in contradiction with the commonly assumed cation distribution given by equation (1.4.1). A

systematic reduction in the proportion of Fe atoms on an A site to zero which would mean that Cd or Zn atoms goes to an A site only, does not occur even at maximum concentration ($x = 1.0$) of these diamagnetic atoms in both series of compounds.

This systematic study of the compounds provides useful information of the evolution of the magnetic and structural properties of the spinel oxides. It is believed that the results presented in this dissertation make a useful contribution to the study of mixed ferrites, worthy of publication [36, 37]. However, the study of the temperature dependence of the materials investigated in this work are not presented. This is all left for a future project as the vibrating sample magnetometer, Mössbauer cryostat and furnace are still being commissioned in the department.

Bibliography

[1] J. Smith and H. Wijn, *Ferrites*, Cleaver–Hume Press, London, 1959, p. 140–154.

[2] T. C. Gibbs, *Principles of Mössbauer Spectroscopy*, Chapman and Hall, London, 1976, p. 22–43, 159–180.

[3] S. C. Bhargawa, A. H. Morrish, H. Kunkel and Z. W. Li, J. Phys.: Condens. Matter. 12 (2000) 9667.

[4] R. S. Tebble and D. J. Craik, *Magnetic Materials*, John Wiley and Sons, London, 1969, p. 252–298.

[5] M. A. Amer, O.M. Hemeda, Hyperfine Interactions 96 (1995) 99.

[6] G. A Pettit, D. W. Forester, Phys. Rev. B 4 (1972) 3912.

[7] H. P. Myers, *Introductory Solid State Physics*, Taylor and Francis, London, 1990, p. 522.

[8] V. T. Thanki, K. H. Jani, B. S. Trivedi, Kunal B. Modi and H. H. Joshi, Materials Lett. 37 (1998) 236.

[9] L. Wang, F. S. Li, J. Magn. Magn. Mater. 223 (2001) 233.

[10] P. G. Bercoff, H. R. Bertorello, J. Magn. Magn. Mater. 213 (2000) 56.

[11] S. R. Elliot, *The Physics and Chemistry of Solids*, John Wiley and Sons, England, 2000, p. 632–640.

[12] M. Amanullah Choudhurry, J. Rahman, J. Magn. Magn. Mater. 223 (2001) 21.

[13] Nitendar Kumar, Y. Purushotham, P. Venugopal Reddy, Z. H. Zaidi, J. Magn. Magn. Mater. 192 (1999) 116.

[14] C. Rath, K. K. Sahu, S. Anand, S. K. Date, N. C. Mishra, R. P. Das, J. Magn. Magn. Mater. 202 (1999) 77.

[15] S. R. Janasi, M. Emura, F. J. Landgraf, D. Rodrigues, J. Magn. Magn. Mater. 238 (2002) 168.

[16] M. R. Singh and S. C. Bhargawa, J. Phys.:Condens. Matter 7 (1995) 8183.

[17] T. Moyo, B. Giordanengo, M. A. C. de Melo, A. Y. Takeuchi, P. R. J. Silva, H. Saitovitch and E. Baggio-Saitovitch, Hyperfine Interactions, 120/121 (1999) 285.

[18] O. M. Hemeda, M. M. Barakat, J. Magn. Magn. Mater. 223 (2001) 127.

[19] B. S Trivedi, R. G. Kulkarni, J. Mater. Sci. 35 (2000) 5523.

[20] X. Liu, W. Zhong, S. Yang, Z. Yu, B. Gu, Y. Du, J. Magn. Magn. Mater. 238 (2002) 207.

[21] S. A. Jadhav, J. Magn. Magn. Mater. 224 (2001) 167.

[22] A. Roy, J. Ghose, A. Ray, R. Rangathan, J. Magn. Magn. Mater. 202 (1999) 359.

[23] D. Ravinder, T. Alivelumanga, Materials Lett. 49 (2001) 1.

[24] A. M. Abdeen, O. M. Hemeda, E. E. Assem, M. M. El–Sehly, J. Magn. Magn. Mater. 238 (2002) 75.

[25] N. N. Greenwood and T. C. Gibbs, *Mössbauer Spectroscopy*, Chapman and Hall, London, 1971, p. 2–18.

[26] G. Burns, *Solid State Physics*, Academic Press, London, 1985, p. 602.

[27] R. H. Jenkins and B. de Vries, *Worked examples in x–ray spectrometry*, Macmillan, London, 1970, p. 124–126.

[28] C. N. Chinnasamy, A. Narayanasamy, N. Ponpandian, R. Justin Joseyphus, B. Jeyadevan, K. Tohji, K. Chattopadhyay, J. Magn. Magn. Mater. 238 (2002) 281.

[29] http://www.mosswinn.com.

[30] http://www.science.uottawa.ca/phy/recoil/.

[31] C. Heck, *Magnetic materials and their applicaions*, Butterworth, London, 1974, p. 203–205.

[32] *Mineral Powder Diffraction File*, JCPDS, USA, 1980, p. 590.

[33] R. C. Weast, M. J. Astle, W. H. Beyer, *Handbook of Chemistry and Physics (65 th Edition 1984–1985)*, CRC Press, Florida, 1985 p. F165.

[34] S. W. Lee, S. Y. An, S. J. Kim, C. S. Kim, J. Magn. Magn. Mater. 239 (2002) 76.

[35] A. H. Morrish and K. Haneda, Ferrites: Proceedings of the 8^{th} International Conference on Ferrites (ICF8), Kyoto and Tokyo, Japan (2000) 247.

[36] J. Z. Msomi, T. Moyo and K. Bharuth-Ram, Hyperfine Interactions (2002) (accepted for publication).

[37] T. Moyo, J. Z. Msomi, and K. Bharuth-Ram, Hyperfine Interactions 136 (3) (2002) 579.